

FIBCD1 is a Conserved Receptor for Chondroitin Sulphate Proteoglycans of the Brain Extracellular Matrix and a Candidate Gene for a Complex Neurodevelopmental Disorder

Christopher W Fell^{1,2,3,†}, Astrid Hagelkruys^{4,†}, Ana Cicvaric^{5,6}, Marion Horrer⁴, Lucy Liu⁷, Joshua Shing Shun Li⁷, Johannes Stadlmann^{4,8}, Anton A Polyansky⁹, Stefan Mereiter⁴, Miguel Angel Tejada^{4,10}, Tomislav Kokotović^{1,2,3}, Angelica Scaramuzza^{1,3}, Kimberly A Twyman¹¹, Michelle M Morrow¹², Jane Juusola¹², Huifang Yan^{13,14}, Jingmin Wang^{13,14}, Margit Burmeister^{15,16}, Thomas Levin Andersen^{17,18}, Gerald Wirnsberger^{4,19}, Uffe Holmskov²⁰, Norbert Perrimon⁷, Bojan Zagrović⁹, Francisco J Monje⁵, Jesper Bonnet Moeller^{20,21}, Josef M Penninger^{4,22*} and Vanja Nagy^{1,2,3*}

¹ Ludwig Boltzmann Institute for Rare and Undiagnosed Diseases, Vienna, Austria.

² CeMM, Research Center for Molecular Medicine of the Austrian Academy of Sciences, Vienna, Austria.

³ Department of Neurology, Medical University of Vienna, Vienna, Austria.

⁴ IMBA, Institute of Molecular Biotechnology of the Austrian Academy of Sciences, VBC – Vienna BioCenter Campus, Vienna, Austria.

⁵ Centre for Physiology and Pharmacology, Department of Neurophysiology and Neuropharmacology, Medical University of Vienna, Vienna, Austria.

⁶ Department of Psychiatry and Behavioral Sciences, Feinberg School of Medicine, Northwestern University, Chicago, IL, USA.

⁷ Department of Genetics, Harvard Medical School, Howard Hughes Medical Institute, Boston, USA.

⁸ Institute of Biochemistry, University of Natural Resource and Life Sciences, Vienna, Austria.

⁹ Department of Structural and Computational Biology, Max Perutz Labs, University of Vienna, Campus Vienna BioCenter 5, A-1030 Vienna, Austria.

¹⁰ Research Unit on Women's Health-Institute of Health Research INCLIVA, Valencia, Spain

¹¹ Mercy Kids Autism Center, Saint Louis, MO, USA.

¹² GeneDx, Gaithersburg, MD, USA.

¹³ Department of Pediatrics, Peking University First Hospital, Beijing, China.

¹⁴ Joint International Research Center of Translational and Clinical Research, Beijing, China.

¹⁵ Michigan Neuroscience Institute, University of Michigan, Ann Arbor, MI, USA.

¹⁶ Departments of Computational Medicine & Bioinformatics, Psychiatry and Human Genetics, University of Michigan, Ann Arbor, MI, USA.

¹⁷ Clinical Cell Biology, Department of Pathology, Odense University Hospital, Odense, Denmark.

¹⁸ Pathology Research Unit, Department of Clinical Research and Department of Molecular Medicine, University of Southern Denmark, Odense, Denmark.

¹⁹ Apeiron Biologics AG, Vienna BioCenter Campus, Vienna, Austria.

²⁰ Cancer and Inflammation Research, Department of Molecular Medicine, University of Southern Denmark, Odense, Denmark.

²¹ Danish Institute for Advanced Study, University of Southern Denmark, Odense, Denmark.

²² Department of Medical Genetics, Life Science Institute, University of British Columbia, Vancouver, Canada.

*Corresponding authors:

Vanja Nagy, vanja.nagy@rud.lbg.ac.at c/o CeMM, Lazarettgasse 14, AKH, BT 25.3, 1090, Vienna, Austria.

Josef M. Penninger, josef.penninger@ubc.ca. Life Sciences Institute, Vancouver Campus, 2350 Health Sciences Mall, Vancouver, BC Canada V6T 1Z3.

†Authors contributed equally

ABSTRACT

The brain extracellular matrix (ECM) is enriched in chondroitin sulphate proteoglycans (CSPGs) with variable sulphate modifications that intimately participate in brain maturation and function. Very little is known about how the changing biophysical properties of the CSPGs are signalled to neurons. Here, we report Fibrinogen C Domain Containing 1 (FIBCD1), a known chitin-binding receptor of the innate immune system, to be highly expressed in the hippocampus and to specifically bind CSPGs containing 4-O sulphate modification (CS-4S). Cultured *Fibcd1* knockout (KO) neurons lack phenotypic and transcriptomic responses to CSPG stimulation. Further, *Fibcd1* KO mice exhibit accumulation of CS-4S, likely resulting in deficits of hippocampal-dependent learning tasks and abrogated synaptic remodelling, a phenotype rescued by enzymatic digestion of CSPGs. Likewise, neuronal specific knockdown of a *Fibcd1* orthologue in flies results in neuronal morphological changes at the neuromuscular junctions and behavioural defects. Finally, we report two undiagnosed patients with a complex neurodevelopmental disorder with deleterious variants in *FIBCD1*, strongly implicating FIBCD1 in the development of the disease. Taken together, our results demonstrate that FIBCD1 is a novel, evolutionarily conserved component of ECM sulphation recognition that is crucial for neuronal development and function.

INTRODUCTION

The brain extracellular matrix (ECM) is a dynamic microenvironment that plays a critical role in the development and maintenance of the nervous system^{1,2}. The ECM is structurally heterogenous and is composed primarily of glycans and glycoconjugates (proteoglycans, glycoproteins and glycolipids). Glycans coordinate and are essential for many neurodevelopmental processes, including axon outgrowth and guidance, synaptogenesis, migration and synaptic plasticity²⁻⁴. There are many inherited human disorders caused by disruptions to the glycosylation pathways. While multiple systems are often affected, most disorders also involve the central nervous system (CNS), with accompanying symptoms including congenital malformations, epilepsy, intellectual disability and developmental delay^{5,6}. Additional connections have been made between altered glycosylation, ECM composition and autism spectrum disorder (ASD), but the molecular mechanisms remain poorly understood⁷.

Proteoglycans are composed of negatively charged glycosaminoglycans (GAGs), which consists of repeating disaccharide units, covalently joined to a core protein. A seminal GAG is chondroitin sulphate (CS), a component of chondroitin sulphate proteoglycans (CSPGs). Different spatiotemporal distributions of CSPGs with variable sulphate modifications correlate with specific and discrete developmental stages as part of the dramatic reorganisation of the ECM that accompanies and regulates brain maturation^{2,8,9}. This includes closure of the ‘critical period’ of heightened synaptic plasticity, when CSPGs condense into lattice-like structures around neurons, known as peri-neuronal nets (PNNs), which restrict juvenile synaptic plasticity and participate in memory formation, retention and extinction^{1,10,11}.

Few cell-surface receptors for CSPGs have been identified. Receptor Protein Tyrosine Phosphatase sigma (PTP σ) and its subfamily member Leukocyte Common Antigen-Related (LAR), as well as the Nogo receptor family members, Nogo66 receptor–1 and 3 (NgR1 and 3) were demonstrated to bind CSPGs¹²⁻¹⁴, however, their role in the brain is unclear. Less is known

regarding recognition of specifically sulphated GAGs on CSPGs. For example, CS-4,6S (or CS-E) recognition was reported for Contactin-1 (CNTN1) and in the lungs for Receptor for Advanced Glycation End Products (RAGE)^{15,16}. RAGE is also associated with Alzheimer pathology¹⁷. Whether CNTN1 or RAGE brain functions are linked to CS-4,6S recognition and the role of CS-4,6S in the brain is poorly understood. To date, associations between disruptions to proteoglycan receptor function and human disease have not been reported.

Here, we identify Fibrinogen C Domain Containing 1 (FIBCD1) as a novel CSPG receptor. Previous work has determined FIBCD1 to be expressed in mucosal epithelial tissues, with highest expression in the human respiratory and gastrointestinal tracts, testes, placenta and brain. FIBCD1 is a type 2 transmembrane protein with high homology to ficolins and has been shown to act as a pattern recognition receptor of chitin, found in the cell walls of fungi¹⁸. FIBCD1 consists of a short N-terminal cytoplasmic tail, transmembrane domain, coiled-coil region through which FIBCD1 forms homotetramers, poly-cationic region and a C-terminal extracellular fibrinogen-related domain (FReD) which participates in ligand interactions¹⁸. FIBCD1 was shown to limit fungal outgrowth, regulate the gut fungal mycobiome and dampen intestinal inflammation^{19,20}. FIBCD1 has also been shown to have an endocytic function and solving of the FReD crystal structure revealed potential binding sites for GAGs such as CS²¹. Despite its high expression in the brain, no function for FIBCD1 in the nervous system has been reported. Here, we demonstrate that FIBCD1 is critical for the function of the nervous system of mice and flies. Additionally, we find *FIBCD1* loss-of-function variants in two unrelated patients contributing to a complex neurodevelopmental disorder (NDD) symptomatology that includes ASD.

RESULTS

***Fibcd1* is expressed in the mouse brain**

As the biological function of FIBCD1 in the CNS has not been explored, we first examined its expression pattern in the mouse brain. *In situ* hybridization (ISH) using complementary DNA probe pairs against *Fibcd1* mRNA in adult mouse coronal brain section revealed strong localisation of *Fibcd1* in the pyramidal cell layer of the hippocampus, granule cells of the dentate gyrus, dispersed cells of the cortex, the medial habenula and hypothalamus (Fig. 1A). Using publicly available datasets of bulk RNA seq of sorted brain cell population, brainrnaseq.org²², we noted *Fibcd1* expression to be highest in neurons, and virtually absent from all other cell types sequenced (Fig. S1A). While RT-qPCR of 6 different brain regions determined that some *Fibcd1* transcripts can be observed in the olfactory bulb as well, expression is highest in the hippocampus (Fig. 1B and Fig. S1B-C). *Fibcd1* transcript levels were high in embryonic mouse brain and dropped to their lowest levels at postnatal day (P) 7 and again increased during postnatal brain development to return to their high embryonic levels at P25 (Fig. 1C and Fig. S1B, D).

***Fibcd1* binds to chondroitin sulphate proteoglycans with a -4S modification**

GAGs of proteoglycans are post-translationally modified by the addition of sulphate groups at different positions by sulfonyletransferases²³. These include, but are not limited to, unsulphated (CS-0S), sulphated at carbon 4 (CS-4S, CS-A) and/or at carbon 6 (CS-6S, CS-C and CS-4,6S, CS-E) comprising the so-called ‘sulphation code.’ As an abundance of CS-4S and CS-6S in the brain ECM was described to be critical for maturation of the brain^{8,24,25}, we sought to determine whether FIBCD1 binds these GAGs as previously hypothesised²¹. Top binding poses for CS-4S and CS-6S were identified using *in silico* molecular docking and an X-ray structure of the

extracellular FReD (PDB 4M7F), followed by post-rescoring of docking solutions as described previously²⁶. According to the scoring function, CS-4S exhibits a better fit to the FReD as compared to CS-6S (45.3 vs 43.3), with the orientations of the two ligands on the FReD surface being nearly orthogonal to each other (Fig. 1D and Fig. S2A). Importantly, the orientation of CS-4S, with its sulphate group packing tightly into a pocket formed by Y405, H415, and Y431 of FReD, leads to a more favourable electrostatic interaction and subsequently lower binding free energy ($\Delta\Delta G$ value of -1.3 kJ mol^{-1}) as predicted by a linear model, published elsewhere²⁷. To characterise binding affinities of FIBCD1 to CS-4S and CS-6S we performed competitive ELISA experiments as described previously¹⁸. Using a previously reported FIBCD1 ligand, acetylated BSA, and increasing concentrations of CS-4S or CS-6S, we determined a strong preference of FIBCD1 to bind CS-4S over CS-6S, with an approximately 10-fold lower IC_{50} concentration of CS-4S compared to CS-6S (Fig. 1E). To assess FIBCD1 binding specificity to CS-4S in a cellular context, we cloned V5-tagged full-length mouse WT *Fibcd1* cDNA and a truncated version without the FReD (*Fibcd1*^{AFReD}) (Fig. S2B). We overexpressed the two FIBCD1 constructs in the mouse N2a cell line and by RT-qPCR and immunoblot analyses confirmed overexpression of FIBCD1 and V5-reactive bands at predicted molecular weights (Fig. S2C-E). We then incubated the cells with fluoresceinamine (FITC)-tagged CS-4S, polysulphated CS (CS-PS) and dermatan sulphate (DS) and acquired the cells by flow cytometry. We determined that cells expressing full length WT *Fibcd1* showed increased V5⁺/FITC⁺ fluorescence intensity in comparison to cells expressing empty vector or *Fibcd1*^{AFReD}, but this was not the case for cells incubated with CS-PS or DS, confirming preferred binding of *Fibcd1*-expressing cells to CS-4S, dependent on the FReD (Fig. 1F).

We next asked whether FIBCD1 is a *bonafide* receptor for CSPGs in hippocampal neurons with high expression of *Fibcd1*. We aimed to determine cellular phenotypic and transcriptomic responses to CSPGs in primary hippocampal cultures. CSPGs are repulsive to neuronal adhesion, neurite outgrowth, growth cone formation, axonal regeneration and

neurogenesis in culture^{12,28}. We reasoned that if FIBCD1 is a receptor for CSPGs, then cells deficient in FIBCD1 would not exhibit the same responses as WT as was shown for canonical CSPG receptors, such as PTP σ previously¹³. We obtained *Fibcd1* KO mice (MGI:5007144²⁹) and validated the absence of *Fibcd1* mRNA transcript in the KO hippocampi (Fig. S3A). The mice were viable, healthy and exhibited no obvious abnormalities (Fig. S3B-D). We harvested primary hippocampal neurons from embryonic (E)18.5 *Fibcd1* WT and KO littermate animals and plated them on coverslips pre-coated with CSPGs containing a mixture of sulphated GAGs. We assessed primary neuronal morphologies after 2 and 14 days *in vitro* (DIV) by analysing cells that stain positive for the neuronal-specific marker Microtubule-associated protein 2 (MAP2). At DIV2, we found the adherence of *Fibcd1* WT neurons was partially abrogated by the presence of CSPG coating, but not in cultures plated on CSPGs after treatment with the enzyme Chondroitinase ABC (ChABC), which cleaves the GAG chains into soluble disaccharides and tetrasaccharides, leaving the core protein intact as described previously (Fig. 2A)^{28,30}. At DIV14, we found a dramatic increase in neuronal somata aggregation in cultures plated on CSPGs, also prevented by ChABC pre-digestion, again in agreement with previous literature (Fig. 2B)²⁸. In contrast, neurons cultured from *Fibcd1* KO hippocampi showed slight, but not significant, DIV2 adherence impairment and slight, but also not significant, DIV14 somata aggregations, indicating that *Fibcd1* KO neurons are resistant to CSPG coating-induced phenotypes. Likely, the residual detection of CSPGs in *Fibcd1* KOs was due to the presence of other CSPG receptors, such as PTP σ ¹³. Taken together, these data confirm FIBCD1 binds GAGs, particularly CS-4S, and mediates CSPG-induced cellular phenotypes.

To investigate transcriptional responses to FIBCD1 binding of CSPGs, we isolated RNA from primary hippocampal neurons plated on coverslips coated with CSPGs (*Fibcd1* WT^{CSPG}, *Fibcd1* KO^{CSPG}) and without (*Fibcd1* WT, *Fibcd1* KO) at DIV3. We performed bulk RNA-sequencing with poly-A enrichment using 4 to 5 biological replicates per condition. We reasoned an early time point after plating transcriptional changes would more likely reflect

cellular developmental effects of FIBCD1-CSPG binding as opposed to secondary effects such as increased cell stress, soma aggregation or dendritic fasciculation. Hierarchical clustering showed small intra-group differences and distinct separation between groups by genotype (WT or KO) and treatment (+/- CSPG) (Fig. S4A). Comparison of differentially expressed genes (DEGs, FDR<0.05) between *Fibcd1* KO and WT cells (without CSPG) revealed 462 significant DEGs with *Fibcd1* being the most downregulated DEG, as expected (Fig. S4B). We noted that a number of the top enriched DEGs in the *Fibcd1* KO vs. WT condition to be genes specifically expressed in non-neuronal cells (e.g. *Pdgfra*, *Olig2*), suggesting that DEGs may be reflecting differences between WT and KO cultures in glia numbers, which are technically challenging to control for. We therefore explored our data further comparing only between conditions within the same genotype, i.e. *Fibcd1* WT^{CSPG} vs WT and *Fibcd1* KO^{CSPG} vs KO.

Comparison between WT^{CSPG} vs WT revealed 462 significant DEGs, of which the majority (396) were downregulated. Comparison between KO^{CSPG} vs KO revealed 345 significant DEGs, of which again the majority (301) were downregulated (Fig. 2C). We cross-referenced DEGs identified in the WT and KO datasets to reveal a set of genes that are responding to CSPGs in both genotypes and those that are dependent on *Fibcd1* expression (Fig. 2D). Among the top dysregulated genes common to both genotypes, independent of *Fibcd1* expression, was *Thbs1*, recently shown to be necessary and sufficient for axon regeneration after injury³¹, normally inhibited by the formation of glial CSPG scars¹³, suggesting that the effects of CSPGs may be mediated by *Thbs1* gene regulation in hippocampal neurons. Many of the remaining genes are involved in binding or remodelling of the actin cytoskeleton (*Acta2*, *Tagln*, *Shroom3*, *Nes*, *Actin*, *Palld*, *Ajuba*, *Flnb*) which reflect the morphological perturbations induced by plating the cells on CSPGs. Gene ontology (GO) term enrichment analysis for downregulated genes revealed terms such as “extracellular matrix binding” and “extracellular matrix structural component” in *Fibcd1* WT cells upon CSPG treatment (Fig. 2E), which suggests that *Fibcd1* not only engages with the components of the

ECM, but also facilitates transcriptional regulation of genes known to play a role in the ECM. Intriguingly, the third-most enriched term was “integrin binding”, reflecting a number of integrin subunits and integrin-related genes that are significantly downregulated in WT cells upon CSPG treatment (Fig. S4C). We next analysed the DEGs unique to the WT cellular response to CSPGs which are dependent on *Fibcd1* expression (Fig. 2D). Among the genes dysregulated in response to CSPGs only in the WT cultures are genes coding for integrin subunits (*Itgal*, *Itgam*), integrin binding and/or modulation (*Adamts8*, *Tln1*)^{32,33}, genes involved in the synthesis or degradation of ECM components (*Adamts8*, *Hspg2*, *Cemip*, *Coll2a1*)³⁴ and, finally, genes involved in binding to the ECM and adhesion of cells to each other and to the ECM (*Flnc*, *Wisp1*, *Tln1*)^{33,35-38}. Together, these genes represent the transcriptional fingerprint of primary hippocampal neurons mediated by *Fibcd1* binding to CSPG.

CS-4S abundance is increased in the *Fibcd1* KO hippocampus

Previous work in a non-neuronal context has shown FIBCD1 to have an endocytic function^{18,21}. Having demonstrated FIBCD1 preferential binds to CS-4S, we hypothesised that FIBCD1 may have a role in endocytosing cell-free extracellular CS-4S and/or CSPGs containing CS-4S in the brain and that a lack of FIBCD1 may cause aberrant accumulation of either or both molecules. Since CSPGs are known to condense into peri-neuronal nets (PNNs), critical for memory formation, retention and extinction^{11,39}, we first looked for any changes in PNNs in the *Fibcd1* KO brain. We found no apparent difference in the hippocampal PNNs between adult WT and KO coronal sections stained with fluorescently-tagged Wisteria floribunda agglutinin (WFA), a lectin that selectively labels CSPGs within PNNs (Fig. 3A)⁴⁰. We also quantified amounts of sulphated GAGs (sGAG) in adult mouse hippocampi lysates, using a 1,9-dimethylmethylene blue based assay (DMMB, which reacts with sGAGs and precipitates) and

found no difference in sGAG amounts between WT and KO samples (Fig. 3B). These data suggest there's no detectable difference in general CSPG levels between *Fibcd1* WT and KO brains. To determine if particularly sulphated GAGs may be accumulating in the absence of FIBCD1 we surveyed the hippocampal glycome composition using high performance liquid chromatography (HPLC) of WT and KO mice hippocampi. HPLC analysis determined a relative increase in the ratio of CS-4S compared to other identified GAGs in the *Fibcd1* KO brains as compared to control littermates (Fig. 3C). Further, Western blot analysis using specific antibodies against differentially sulphated GAGs determined a significant increase of CS-4S abundance in the *Fibcd1*KO hippocampi as compared to controls, while CS-0S and CS-6S remained unchanged (Fig. 3D). These data indicate that while total GAG levels and overall WFA-reactive PNN-associated CSPG abundance remain unchanged, FIBCD1 deficiency leads to a specific accumulation of GAGs containing CS-4S in the hippocampus, possibly due to an inability of cells to bind and endocytose CS-4S GAGs.

***Fibcd1* deficiency leads to defects in hippocampal-dependent learning and long-term potentiation in mice**

To determine the behavioural consequences of CS-4S accumulation in the *Fibcd1* mouse model, we subjected *Fibcd1* WT and KO adult mice to a series of hippocampal-dependent learning tasks. Additionally, 15T MRI volumetric analysis revealed no significant differences in total brain volume, or 11 other isolated brain regions as compared to control littermates determining no overt structural abnormalities in the brains of mice with a FIBCD1 deficiency (Fig. S3D). Behaviourally, we first established that there is no difference in baseline anxiety levels between *Fibcd1* WT and KO mice as assessed by the Elevated Plus Maze (EPM) (Fig. S5A). We also detected no difference in the acquisition and retention of spatial learning between *Fibcd1* WT and KO mice, as assessed by the Morris Water Maze (MWM) (Fig. S5B-

C). Nociceptive responses to noxious chemicals or heat stimulation revealed no deficiencies in sensory nervous system processing of acute pain (Fig. S5D). However, we found that *Fibcd1* KO mice were significantly impaired in spatial working memory as assessed by spontaneous alternation in the Y-Maze (Fig. 4A). Further, we found that *Fibcd1* KO animals were significantly impaired in fear-associated learning, as assessed by inhibitory avoidance (IA) task, compared to WT and heterozygous animals (Fig. 4B). Taken together, and in line with high expression of *Fibcd1* in the hippocampus, these data suggest that FIBCD1 is essential for proper mouse hippocampal development and/or function.

***Fibcd1* deficiency induced synaptic dysfunction are rescued by CSPG digestion**

To validate our behavioural findings and ascertain the possible effects of CS-4S accumulation in synaptic function we next performed field recordings of acute hippocampal slices from adult *Fibcd1* WT and KO mice pre-incubated with ChABC or penicillinase (Pen, a treatment control that has no endogenous substrate in the brain). We hypothesised that deficiencies caused by the accumulation of GAGs containing CS-4S in the *Fibcd1* KO hippocampus could be rescued by digestion with ChABC, as is the case with other neuropathies associated with increased CSPG levels (e.g. Alzheimer's disease^{41,42}).

Therefore, we examined the electrical properties of the CA3 Schaffer-collateral to CA1 circuit, a key pathway implicated in the formation and maintenance of spatial memories⁴³. We first analysed basal properties of synaptic transmission using standard input/output protocols and found no significant differences between all conditions (Fig. S5E-F), indicating the ChABC treatment does not alter the properties of basal synaptic transmission in agreement with previous literature⁴⁴ and indeed, no differences between pen-treated *Fibcd1* WT and KO hippocampi. We next examined paired-pulse-induced facilitation, a form of short-term pre-synaptic plasticity directly related to neurotransmitter release⁴⁵. We observed no differences between

Pen or ChABC treated WT slices, in agreement with previous literature⁴⁴. However, slices obtained from KO mice and treated with Pen showed reduced paired-pulse-facilitation compared to Pen-treated WT slices (Fig. 4C-D). Remarkably, this reduction was restored to WT levels in the ChABC-treated KO slices (Fig. 4C-D). Finally, we examined the effects of theta-burst stimulation (TBS) induced synaptic long-term potentiation (LTP) such as the kind recorded during learning events in mice. Consistent with previous literature^{44,46}, ChABC treatment reduced, but did not abolish, potentiation in WT slices, starting at the first recorded pulse (Fig. 4E, blue traces). We found slices from KO mice pre-treated with Pen to exhibit reduced potentiation similar to WT ChABC-treated slices (Fig. 4E, dark blue vs dark red traces), but, remarkably, this deficit was again rescued in KO slices pre-treated with ChABC (Fig. 4E, pink trace and Fig. S5G-H).

Fibcd1 neuronal function is evolutionarily conserved in *Drosophila melanogaster*

We next investigated if the role of Fibcd1 in the nervous system is conserved in other species. *CG10359* is a putative Fibcd1 orthologue in *Drosophila melanogaster* (*D. melanogaster*), with a high degree of FReD amino acid sequence homology (Fig. S6A) between human and mouse Fibcd1 and *D. melanogaster* *CG10359* (hereafter referred to as *dFibcd1*). As of yet, *dFibcd1* has no assigned function. To assess the function of *dFibcd1*, we performed RNA interference (RNAi)-mediated *dFibcd1* knockdown. We crossed three independent RNAi constructs targeting *dFibcd1* (downstream of *UAS* promoter sequence, hereafter as lines #1, #2 and #3) with lines expressing *GAL4* under the control of either the tubulin (*tub*) promoter for whole body RNAi expression or the neuronal *Synaptobrevin* promoter (*Nsyb*) for neuronal expression of RNAi. Full body knockdown of *dFibcd1* was lethal or semi-lethal in 2 of 3 lines (Fig. S6B), so we proceeded only with flies with neuronal knockdown of *dFibcd1*.

Neuronal knockdown of *dFibcd1* resulted in abnormal neuronal development, visualized in neuronal morphology at the larva neuromuscular junction (NMJ) (Fig. 4F). All neuronal RNAi lines exhibited reduced number of pre-synaptic boutons (Fig. 4G) and line 3 further exhibited reduced degree of neuronal branching, suggesting a reduction in neuronal function (Fig. 4H). To assess if these developmental defects also manifested as neurological phenotypes in adults, we assessed the climbing behaviour of these flies by negative geotaxis assay. We found that neuronal knockdown of *dFibcd1* resulted in reduced climbing ability when compared to control flies expressing control RNAi targeting luciferase (Fig. 4I and Fig. S6C). Taken together, our results suggest a critical role for *Fibcd1* in *D. melanogaster* survival and neuronal development and function.

Characterisation of human FIBCD1 expression and function

We next asked whether the expression and function of *Fibcd1* is conserved in humans. We profiled *FIBCD1* expression using a cDNA array from 48 different human tissues and determined that the brain is the third highest *FIBCD1* expressing tissue in humans (Fig. 5A). A further *FIBCD1* gene expression analysis of cDNA array from 24 different human brain regions determined that *FIBCD1* expression is highest in the hippocampus, followed by the hypothalamus and cortex, very similar to the *Fibcd1* expression profile in the mouse brain (Fig. 5A, inset). Considering FIBCD1's function in mouse brain and the similarity of expression of *Fibcd1* transcripts in human and mouse CNS, we reasoned that patients with deleterious variants in *FIBCD1* would suffer from neurological dysfunctions. To our knowledge, there are no genetic disorders associated with variants in FIBCD1 to date. The Genome Aggregation Database (gnomAD⁴⁷) that documents sequenced human genetic variants, reports 266 variants annotated as missense, stop-gained, frameshift or splice disrupting within the *FIBCD1* gene (Fig. S7A). As gnomAD does not report on zygosity or health status of any sequenced

individual in the database, we searched for undiagnosed rare disease patients with high Combined Annotation Dependent Depletion (CADD) scoring variants in *FIBCD1* within our network and through GeneMatcher⁴⁸ and were able to locate 2 unrelated patients with undiagnosed neurodevelopmental disorders. Patient 1 (P1) is a 12 year old nonverbal male from a Caucasian non-consanguineous family (Fig. 5B), with severe autism spectrum disorder (ASD), delayed verbal cognition, anxiety and attention deficit hyperactivity disorder (ADHD). He has high pain tolerance, fine motor coordination deficits and mild facial dysmorphism. Additionally, he experiences frequent allergic rhinitis and sinusitis (Table 1). There is no history of neurological disease in the family, however, several members of the maternal family have learning disabilities. As part of his clinical diagnostic evaluation, whole exome sequencing (WES) was performed at GeneDx, USA (www.genedx.com) and identifying compound heterozygous variants in *FIBCD1* Chr9:133805421 C>T; c.85 G>A; p.(G29S) and Chr9:133779621 G>A; c.1216C>T; p.(R406C), with CADD scores of 6.832 and 25.1, respectively, and a *de novo* variant in *CSMD3* Chr8: 113933925 T>C; c.1564 A>G; p.(K522E) with a CADD score of 24.7. While *CSMD3* variants have been reported in association with neurodevelopmental disorders, most published missense variants have population data in gnomAD or internal data at GeneDX, reducing the likelihood that this variant is related to the phenotype (⁴⁹; GeneDX, Inc. personal communication). Therefore, the *FIBCD1* variants were prioritised for further analysis. Sanger sequencing determined each variant was inherited from one of the parents (Fig. 5B). There were no other variants with confirmed association to human disease identified that would match the phenotype or inheritance pattern. Patient 2 (P2) is a nonverbal 3 year old Chinese female from a non-consanguineous family with no history of genetic neurological disease (Fig. 5B), that presented with severe neurodevelopmental disorder (NDD), delayed social and cognitive abilities and delayed sitting and walking. Magnetic resonance imaging (MRI) revealed thickened cortex, decreased white/grey matter ratio, bilateral enlarged frontal gyri and ventriculomegaly (Fig. 5C). The patient also has

microcephaly and dysmorphic facial features (Table 1). Additionally, recurrent pneumonia was also noted. Clinical genetic testing was performed and revealed inheritance by uniparental disomy (UPD) with mosaicism. Homozygous variants of unknown significance were found in *FIBCD1* Chr9:133779470 G>A; c.1367C>T; p.(P456L) with a CADD score of 29, *UNC13B* Chr9:35376187; c.1531T>C; p.(C511R) with a CADD score of 28.4, and *RIC1* Chr9:5765523; c.2951C>T; p.(A984V) with a CADD score of 28.6. Variants within *UNC13B* and *RIC1* were deprioritised from further functional studies due to a lack of clinical similarities with published cases⁵⁰⁻⁵².

To determine whether the *FIBCD1* variants found in these patients affect protein folding or function we first performed all-atom molecular dynamics (MD) simulations in the microsecond range of the two *FIBCD1* variants contained within the FReD domain (p.R406C and p.P456L) and the WT as control. In the course of MD simulations, both WT and patient variant conformations stay relatively close to the initial structure, with the backbone root-mean-squared-deviations (RMSD) being the highest for R406C, intermediate for P456L and the lowest for WT (Fig. S7B), but never exceeding 2.5 Å. In order to compare WT and the two mutant structures, the dominant MD conformations were identified using structural clustering. The dominant P456L and R406C structures, deviate from the dominant WT structure by 1.6 Å and 1.5 Å backbone RMSD, respectively, while being relatively more similar to each other (1.2 Å). The largest structural rearrangements induced by the variants take place in the 389-399 and 423-448 loop regions, which surround the ligand binding site (Fig. 5E). Here, the R406C variant has a direct effect due to a disruption of the salt bridge between R406 and D433, which in the WT likely stabilises the mutual arrangement of the two loop regions. In the case of the P456L variant, the effect is rather allosteric, whereby perturbation of the conformational dynamics of the C-terminus, likely due to the removal of the sterically restricted P456, is transmitted towards the upstream 423-448 loop region. Importantly, the similar structural effect of both variants is connected to a similar perturbation of the electrostatic properties on the protein surface in the

vicinity of the ligand binding site. In particular, both variants significantly increase the negative charge density of the surface patch surrounding the ligand binding site (especially R406C), in stark contrast with the WT where the corresponding surface is positively charged (Fig. 5E). We expect that this perturbation significantly weakens the binding of negatively charged phosphorylated ligands by the mutated FReDs.

To substantiate these observations, we generated HEK293T cell lines stably overexpressing FLAG-tagged human WT FIBCD1 cDNA and each of the variants G29S, R406C and P456L, as well as the W6* variant located in gnomAD database (Fig. S7A) which generates a premature STOP codon at the 6th amino acid of FIBCD1, and results in a non-functional protein that serves as a negative control. We confirmed expression in each overexpressing cell line, barring W6*, by immunofluorescence (Fig. S7C). We next asked if the variants identified in our patients functionally perturbed FIBCD1:CS-4S binding, as indicated by the molecular dynamics study. We incubated HEK293T cells overexpressing WT, W6*, G29S, R406C and P456L FIBCD1 cDNAs with FITC-tagged CS-4S and acquired by flow cytometry. As with mouse WT Fibcd1 we determined that cells expressing full length human WT FIBCD1 showed increased percentage of FITC⁺ cells relative to unstained cells (Fig. 1F) or cells expressing FIBCD1_W6*. Intriguingly, this was not the case for cells expressing any of the patient variants, which exhibited similar percentage of FITC⁺ cells as the untransduced control (Fig. 5F). Together these data suggest that while the *FIBCD1* variants identified in patients did not affect protein expression, they disrupted the binding of FIBCD1 to CS-4S. Further, our molecular docking experiments suggest that, for the R406C and P456L variants, the disturbed binding may be due to a disruption of the surface electrostatic charge of the CS-4S binding pocket of FIBCD1's FReD. Taken together, we conclude that P1 and 2 carry variants deleterious to FIBCD1 function potentially contributing to their symptoms and reveal FIBCD1 as a novel candidate gene for NDD.

382

383 DISCUSSION

384 Here we report that FIBCD1, highly expressed in the mammalian brain, is a novel receptor of
 385 CSPGs, which preferentially binds to CS-4S GAGs and mediates a transcriptional program
 386 required for cell-cell and cell-matrix interactions. Using genetically modified mice and flies,
 387 we find that FIBCD1 is critical for neuronal maturation and function, whose downregulation
 388 leads to neurodevelopmental impairments and hippocampal-dependent learning deficiencies,
 389 likely resulting from aberrant accumulation of CS-4S. Additionally, we have identified 2
 390 unrelated patients with complex NDDs that include ASD, carrying deleterious variants within
 391 the *FIBCD1* gene, implicating FIBCD1 as critical to CNS development in humans and as a
 392 novel risk gene for NDDs.

393 FIBCD1 is an endocytic lectin, reported to bind chitin on cellular walls of pathogens
 394 and to regulate the innate immune response to candida infections^{18,19}. We provide
 395 computational, biochemical, cellular and *in vivo* evidence that FIBCD1 also has endogenous
 396 ligands in the brain and intimately participates in the regulation of ECM composition through
 397 endocytosis or receptor-mediated signalling, or both. Indeed, transcriptomic changes upon
 398 CSPG stimulation of *FIBCD1* WT and KO primary hippocampal cultures reveal a novel ligand-
 399 dependent signalling function for FIBCD1, primarily encompassing genes involved in ECM
 400 binding and structure. Interestingly, a number of DEGs were integrin subunits or integrin-
 401 related genes, molecules well known for interacting with the ECM and signalling during
 402 neuronal development and synaptic activity^{1,4}. Considering that closely related proteins
 403 containing FReDs have been shown to directly interact with integrins⁵³, it is tempting to
 404 speculate a physical Fibcd1:integrin interaction, the mechanism of which remains to be
 405 uncovered. We cross-referenced the DEGs present in both the WT^{CSPG} vs WT and KO^{CSPG} vs
 406 KO datasets to identify the genes specifically regulated by Fibcd1 binding to CSPGs. We
 407 identified a number of genes coding for integrin subunits or integrin binding and/or modulation

as well as genes involved in the synthesis or degradation of ECM components and, finally, genes involved in binding to the ECM and adhesion of cells to the ECM. While the functions of many of these genes have been elucidated in a non-neuronal context, it's likely that their function is largely conserved in neurons and, therefore, these genes make up the transcriptional fingerprint regulated by *FIBCD1*'s interaction with CSPGs in primary hippocampal neurons.

The accumulation of CS-4S in the *Fibcd1* KO mouse hippocampi, and the ChABC-mediated rescue of LTP, strongly support the primary role of *FIBCD1* as an endocytic receptor. However, it is unclear whether *FIBCD1* binds entire CSPGs or its specifically sulphated GAG components and how this binding activates transcriptomic changes noted in neuronal cultures *in vivo*. The complete rescue of LTP deficits by ChABC digestion of CSPGs suggests that the hippocampus develops normally in the absence of *FIBCD1* and it is the pathological accumulation of GAGs containing CS-4S over time that is responsible for the observed behavioural and synaptic phenotypes. This is in contrast to the dependence of *dFibcd1* expression in *D. melanogaster* survival and neuronal development as exhibited by the lethality of the full body *dFibcd1* knock-down flies, suggesting that *Fibcd1* may have developed a more specialised role in mammals. Nevertheless, it will be of great interest to delineate the role of CS-4S during activity-driven synaptic activity, in what context it is released from the ECM and how it contributes to hippocampal function.

It is widely recognised that brain ECM composition is critical for CNS development and function and there is growing evidence that deleterious variants in genes encoding glycoproteins, enzymes involved in glycosylation, or those required for their clearance and degradation contribute to neurodevelopmental dysfunctions, such as ASD⁷. Here, we presented evidence for an additional risk gene, *FIBCD1*, in two patients that exhibit symptoms of severe neurodevelopmental dysfunctions, including delayed social, cognitive and verbal abilities, ASD, ADHD, facial dysmorphias and structural brain anomalies. P2 was too young at last

examination to be fully evaluated for ASD or ID, however, while exhibiting similar symptoms as P1, was more affected. Intriguingly, signs of immune system dysfunction such as recurring allergic rhinitis, sinusitis and pneumonia in both patients is in line with the literature describing FIBCD1 in immune responses⁵⁴. In addition to *FIBCD1* variants, P2's exome sequencing revealed additional variants of unknown significance (VUS) in *UNC13B* and *RIC1*. *UNC13B* encodes a pre-synaptic protein highly expressed in the brain, MUNC13-2, that has recently been associated with partial focal epilepsy⁵², not found in P2, and was therefore dismissed as potentially causative in this case. Variants in *RIC1* gene have recently been associated with autosomal recessive CATIFA Syndrome (cleft lip, cataract, tooth abnormality, intellectual disability, facial dysmorphism, attention-deficit hyperactivity disorder, OMIM: 618761)^{50,51}. With the exception of P2's micrognathia, she exhibits none of the hallmark symptoms of CATIFA syndrome (cleft lip, cataracts, tooth abnormalities). However, the contribution of the *RIC1* variant to the overall clinical pathology of the patient cannot be ruled out, even if unlikely.

In silico molecular simulation studies and cellular assays have determined the deleteriousness of the identified *FIBCD1* variants. Molecular modelling analysis has suggested that the FReD variants, R406C (P1) and P456L (P2), both lead to FIBCD1 loss-of-function by disrupting the binding pocket's electrostatic charge and diminishing the affinity to its GAG ligand, which is consistent with our cellular assay for FIBCD1:CS-4S binding. However, it is less clear how the other P1 variant, G29S, disrupts binding of FIBCD1 to CS-4S. While we find the glycine at this residue is largely conserved among other species, the mouse orthologue contains the same substitution of glycine to serine as in P1, yet this substitution in the human *FIBCD1* orthologue was similarly disruptive of binding to GAGs as the other variants. How the function of G29 residue diverges from mouse to human, whether it is important for structural confirmation of FIBCD1, targeting, or downstream signalling remains to be elucidated. Nevertheless, we demonstrated all three FIBCD1 variants to be deleterious to protein function

of FIBCD1 and in view of the data in the model organisms and cell culture, is likely to be causative of the patients' symptoms. Full understanding of the neuropathology caused by deleterious *FIBCD1* variants awaits more clinical cases for comparison of their clinical symptoms.

Overall, FIBCD1 is a regulator of CS-4S content in the hippocampal ECM and a mediator of ECM signalling. FIBCD1 is a critical regulator of synaptic plasticity events underlying certain types of learning and memory in mice and a novel risk gene for a complex form of neurodevelopmental disorder.

AUTHOR CONTRIBUTIONS

Conceptualisation: V.N. Formal Analysis: C.W.F., A.H., A.C., L.L., J.S.S.L., M.A.T., T.K., S.M., J.S., A.A.P., A.S., M.M.M., J.J., J.B.M., V.N. Funding Acquisition: J.P., V.N. Investigation: C.W.F., A.H., A.C., L.L., J.S.S.L., M.A.T., M.H., S.M., J.S., A.A.P., A.S., K.A.T., H.Y., J.W., T.L.A., G.W., J.B.M., V.N. Resources: N.P., B.Z., F.Q.M., J.B.M., J.M.P., V.N. Supervision: U.H., N.P., B.Z., F.Q.M., J.B.M., J.M.P., V.N. Visualisation: C.W.F., A.H., A.C., M.H., L.L., J.S.S.L., S.M., M.A.T., J.S., A.A.P., J.B.M., V.N. Writing – original draft: C.W.F., V.N., with contribution from all authors.

ACKNOWLEDGMENTS

We thank Malene Hyggelbjerg Nielsen for excellent technical assistance with the ISH data. We are thankful to all members of the IMP-IMBA Bio-optics Core Facility for assistance in cell sorting and imaging as well as the Molecular Biology Service for their help. Moreover, we thank the Preclinical Phenotyping Facility, the Preclinical Imaging Facility and the Next

484 Generation Sequencing Facility at the Vienna BioCenter Core Facilities GmbH (VBCF),
485 member of Vienna BioCenter (VBC), Austria.

486 C.W.F. is funded by a DOC fellowship of the Austrian Academy of Sciences (OeAW):
487 25525; L.L. is a fellow of the Damon Runyon Cancer Research Foundation (DRG-2319-18);
488 S.M. is funded by the European Union's Horizon 2020 research and innovation programme
489 under the Marie Skłodowska-Curie grant agreement No. 841319; J.B.M. is funded by the Novo
490 Nordisk foundation; J.M.P. is supported by the Austrian Federal Ministry of Education, Science
491 and Research, the Austrian Academy of Sciences and the City of Vienna and grants from the
492 Austrian Science Fund (FWF) Wittgenstein award (Z 271-B19), the T. von Zastrow foundation,
493 and a Canada 150 Research Chairs Program (F18-01336); V.N. is funded by Ludwig Boltzmann
494 Gesellschaft core funding.

497 **DECLARATIONS OF INTEREST**

498 J.J. and M.M.M. are employees of GeneDx, Inc.

MATERIALS AND METHODS

Patients and Whole Exome Sequencing

All procedures were performed following informed consent and approval from patients and relatives.

Patient 1

Using genomic DNA from the proband and parents, the exonic regions and flanking splice junctions of the genome were captured using the IDT xGen Exome Research Panel v1.0 (Integrated DNA Technologies, Coralville, IA). Massively parallel (NextGen) sequencing was done on an Illumina system with 100bp or greater paired-end reads. Reads were aligned to human genome build GRCh37/UCSC hg19, and analysed for sequence variants using a custom-developed analysis tool. Additional sequencing technology and variant interpretation protocol has been previously described⁵⁵. The general assertion criteria for variant classification are publicly available on the GeneDx ClinVar submission page (<http://www.ncbi.nlm.nih.gov/clinvar/submitters/26957/>).

Patient 2

Procedures were in accordance with the ethical standards and approval of the Medical Ethics Committee of Peking University First Hospital. The IRB number is No. [2005]004. Patients were sequenced and analysed as described previously⁵⁶, with sequencing performed by Joy Oriental Co. (Beijing, China).

Population Genetics

CADD scores and amino acid positions for FIBCD1 variants present in the population were extracted from GnomAD⁴⁷ and visualised using PopViz⁵⁷.

526

527 Animals

528 *Mus musculus*

529 Fibcd1tm1Lex mice (MGI: 5007144)²⁹ were bred on a C57BL/6J genetic background. Mouse
530 genotypes were assessed by PCR (see Supplementary Table 1 for genotyping primer
531 sequences). Of note, only age- and sex-matched littermates from respective crosses were used
532 for experiments. All mice were housed at the Comparative Medicine Mousehouse Vienna
533 BioCenter, Vienna, Austria, maintained at a 12-h light/dark cycle and provided with food and
534 water *ad libitum*. Experiments were approved by the Bundesministerium für Wissenschaft,
535 Forschung und Wirtschaft (BMFWF-66.009/0048-WF/V/3b/2018) and carried out according
536 to EU-directive 2010/63/EU.

537

538 *Drosophila melanogaster*

539 All studies were performed in age, light, sex and temperature matched flies. All crosses were
540 raised at 25°C on standard molasses fly food unless otherwise noted.

541

542 In situ hybridisation

543 The brain tissue was dissected from two 8-10 weeks old C57B6J mice and fixed in buffered 4%
544 paraformaldehyde, dehydrated and paraffin-embedded. 3.5-µm-thick frontal sections were *in*
545 *situ* hybridized with an enhanced RNAScope 2.5 high-definition procedure (310035, ACD
546 Bioscience), as described previously⁵⁸. The sections were hybridized with 20 probe pairs for
547 mouse *Fibcd1* mRNA (524021, ACD Bioscience, targeting nucleotide 629 – 1567) or probe
548 diluent as negative control. The probe pairs were branch amplified as instructed by the
549 manufacturer, and further tyramide-enhanced using digoxigenin-conjugated tyramide
550 (NEL748001KT, PerkinElmer) followed by alkaline phosphatase-conjugated sheep anti-
551 digoxigenin FAB fragments (11093274910, Roche) and visualization with Liquid Permanent

Red (Agilent Technologies). Finally, the sections were counterstained with Mayer's hematoxylin.

RNA-sequencing

RNA was isolated using Qiagen RNeasy Mini kit (74104). Library prep, sequencing and alignment were done at the Vienna BioCenter Next Generation Sequencing Facility. RNA was quantified on a Qubit Fluorometric Quantitation system (Life Technologies) and RNA integrity score calculated using a Bioanalyzer (Agilent). Poly-A enrichment was performed using NEBNext Poly(A) mRNA Magnetic Isolation Module (NEB #E7490) and library prep performed using NEBNext Ultra II Directional RNA Library Prep Kit for Illumina (NEB #E7760) and sequenced on an Illumina HiSeq 3000/4000, 50bp single-read.

RNA-seq analysis

Demultiplexing, quality control, and alignment to the genome was done by the VBC Next Generation Sequencing Facility (Vienna, Austria). Calculation of differentially expressed genes (DEGs) was performed using Bioconductor DESeq2 package⁵⁹. All DEGs located on the X or Y chromosomes were excluded due to uncontrollable distributions of male and female E18.5 pups from which hippocampal neurons were harvested. Sequencing data was uploaded and analysed on the Galaxy web platform (www.usegalaxy.eu)⁶⁰. GO term enrichment analysis was performed using WebGestalt⁶¹, over-representation analysis method.

RT-qPCR

Mouse

For mouse *Fibcdl* expression analysis by RT-qPCR, tissues and cells were isolated and homogenized in TRIzol reagent (Invitrogen). Total RNA was isolated according to the manufacturer's instructions. RNA was reverse transcribed with the iScript cDNA synthesis kit

(Bio-Rad). Real-time PCR analysis was performed with GoTaq qPCR master mix (Promega) on a CFX384 system (Bio-Rad). Data were normalized to values for the housekeeping gene *Gapdh*. See Supplementary Table 1 for a list of primers used in this study.

Human

Human cDNA panels were obtained from Origene: TissueScan, Human Brain cDNA Array (#HBRT101), TissueScan, Human Normal cDNA Array (#HMRT304). Master mixes containing primer pairs against *FIBCD1* or *B2M* (Beta-2-microglobulin, housekeeping gene) were prepared with iTaq Universal SYBR Green Supermix (Bio-Rad #1725122). The mastermixes were dispensed into each well containing cDNA and incubated on ice for 15 minutes to allow the cDNA to dissolve, then briefly vortexed. Reactions were run on Applied Biosystems StepOne Plus machine with standard settings including the melt curve. Data were normalised to values for the housekeeping gene *B2M*. See Supplementary Table 1 for a list of primers.

In Silico Modelling of FIBCD1

Docking

In silico molecular docking was performed using GOLD software version 5.2.2⁶² and an X-ray structure of the extracellular FReD (PDB 4M7F)²¹. The post-rescoring of docking solutions (100 in total) was carried out as described previously²⁶. The binding free energy of CS-4S and CS-6S to FReD domain was estimated using PRODIGY-LIGAND²⁷ after refinement of the complexes using HADDOCK2.2 web-server⁶³.

Patient Variant Modelling

The initial protein configuration was taken from the X-ray structure of the FReD (PDB: 4M7F; aa 239-458), where single point mutations R406C and P456L were introduced using PyMol⁶⁴.

604 The WT and the two mutant structures were used for further all-atom molecular dynamics (MD)
605 simulations in rectangular boxes ($6 \times 6 \times 6 \text{ nm}^3$) filled with ~ 6000 explicit water molecules. A
606 total of 1 μs of MD statistics was collected for each system. All MD simulations and the analysis
607 were performed using GROMACS 5.1.4 package⁶⁵ and Amber99SB-ILDN force field⁶⁶. After
608 initial energy minimization, all systems were solvated using TIP3P water model⁶⁷. The solvated
609 systems had neutral net charge and effective NaCl concentration of 0.1 M. These systems were
610 again energy-minimized and subjected to an MD equilibration of 30000 steps using a 0.5 fs
611 time step with position restraints applied to all protein atoms (restraining force constants
612 $F_x=F_y=F_z=1000 \text{ kJ mol}^{-1} \text{ nm}^{-1}$) and 250000 steps using a 1 fs time step without any restraints.
613 Finally, production runs were carried out for all systems using a 2 fs time step. A twin-range
614 (10/12 Å) spherical cut-off function was used to truncate van der Waals interactions.
615 Electrostatic interactions were treated using the particle-mesh Ewald summation with a real
616 space cutoff 12 and 1.2 Å grid with fourth-order spline interpolation. MD simulations were
617 carried out using 3D periodic boundary conditions in the isothermal–isobaric (NPT) ensemble
618 with an isotropic pressure of 1.013 bar and a constant temperature of 310 K. The pressure and
619 temperature were controlled using Nose-Hoover thermostat⁶⁸ and a Parrinello-Rahman
620 barostat⁶⁹ with 0.5 and 10 ps relaxation parameters, respectively, and a compressibility of 4.5
621 $\times 10^{-5} \text{ bar}^{-1}$ for the barostat. Protein and solvent molecules were coupled to both thermostat
622 and barostat separately. Bond lengths were constrained using LINCS⁷⁰. Root-mean-squared
623 deviations (RMSD) from the starting configuration were calculated using *rms* utility
624 (GROMACS) over all backbone atoms. Conformational clustering of MD trajectories was
625 performed using *cluster* utility (GROMACS) with the applied RMSD cut-off for backbone
626 atoms of neighboring structures of 0.9 Å – a minimum value at which only a single dominant
627 state was identified for WT. Electrostatic potential was calculated and mapped onto the protein
628 solvent accessible surface using the APBS web-service (<https://server.poissonboltzmann.org>)⁷¹.
629 Protein structures were visualized using PyMol⁶⁴.

Binding assays

Characterisation of FIBCD1 binding specificity to chondroitin sulphate 4S (CS-4S) and chondroitin sulphate 6S (CS-6S) was performed through ELISA-based inhibition experiments essentially as described previously¹⁸. In brief, microtiter plates (MaxiSorp, NUNC) were coated with 1 µg/ml acetylated BSA (Sigma) and blocked with TBS containing 0.05% Tween. Recombinant FIBCD1-FReD¹⁸ was added to each well in a constant concentration of 100 ng/ml in TBS containing 0.05% Tween and 5mM CaCl₂ together with 2-fold dilutions of CS-4S and CS-6S (Amsbio). After incubation overnight at 4°C and washing, the wells were incubated for 2 hours at room temperature with 1 µg/ml biotinylated anti-FIBCD1 (clone 11-14-25), before washed and developed using HRP-conjugated streptavidin and TMB substrate.

Tissue Culture

Primary Neurons

Timed pregnancy E18.5 pups were sacrificed by decapitation, the hippocampi dissected into 1x Hank's Buffered Saline Solution (HBSS, Gibco #14185045) with 100 U/ml penicillin/streptomycin (Biowest #L0022-020). The tissue was minced, incubated with trypsin (0.025%) for 15 minutes at 37°C, inverting every 5 mins, and the trypsin inactivated with 10% FCS-containing media. The tissues were then washed 3 times with HBSS and triturated with heat-polished glass pipettes. 200,000 dissociated cells were plated in 1 ml of Neurobasal medium (ThermoFisher #21103049) supplemented with 10% FCS, 2mM L-glutamine (Gibco #25030149), 1x B27 (Gibco #17504001), 10mM Hepes (Gibco #15630056), 100 U/ml pen/strep in a 12-well plate and incubated at 37°C, 5% CO₂. 50% of media was exchanged to FCS-free medium after 24 hours and then every 36 hours. Cells were plated on coverslips coated with 0-4µg/ml CSPGs (Merck #CC117) with and without prior ChABC (Sigma-Aldrich C3667) digestion as described previously^{13,28}.

FIBCD1 overexpression

Mouse

Fibcd1 mouse cDNA with 3' V5 tag was ordered as a G-block from IDT and cloned along with ΔFReD construct via restriction enzyme insertion cloning, using 5' XhoI and 3' EcoRI restriction enzyme sites. The constructs were cloned into a custom pMSCV-IRES-mCherry plasmid, see supplementary data for construct sequences.

Fibcd1 constructs were packaged into virus by CaCl₂ transfecting 70-80% confluent 10cm² plate of Platinum-E (PlatE) HEK 293T cells (Cell Biolabs #RV-101) with 10μg Fibcd1 construct and 2μg gag/pol plasmid. The media was exchanged next day to remove transfection mixture. N2a cells' media was exchanged with virus-containing supernatant at 48- and 72-hours post-transfection with 8μg/ml polybrene (Sigma #H9268). N2a cells were expanded and FACS sorted for mCherry+ cells.

N2a cells stably expressing full-length V5-tagged FIBCD1, FIBCD1 lacking the fibrinogen domain (ΔFReD) or the empty vector (pMSCV-IRES-mCherry) were grown in DMEM supplemented with 10% foetal calf serum, 100 U/ml penicillin (Sigma) and 100μg/ml streptomycin sulphate (Sigma).

Human

hFIBCD1 cDNA was ordered from Origene (#RC206180) and sub-cloned by Gateway cloning (Thermo) into a custom plasmid (via pDONR201) with 3' 3xFLAG tags, mCherry and Blasticidine resistance selection markers, sequences are available in supplementary data. The PCR primers before the BP reaction were designed to remove the 3' STOP codon present in the Origene clone to allow read-through to the 3' 3xFLAG tags. Point variants were introduced into *hFibcd1* cDNA while cloned in the intermediate pDONR201 plasmid using the Q5 site-directed mutagenesis kit (NEB #E0554), following the manufacturer's protocol, and the resultant clones

sequenced to confirm correct base substitution before continuing to the LR reaction into the destination plasmid.

Cloned plasmids were packaged in Lenti-X 293T cells (Takara Biosciences #632180), transfected using Lipofectamine 2000 (Thermo #11668027), following the manufacturer's protocol. Per well of a 6 well plate, 1200ng of Fibcd1 plasmid was mixed with 150µl Opti-Mem (Gibco #31985062), 700ng pGag/pol, 460ng pVSVg and 280ng pAdVantage (Promega #E1711) and transfected for 6-8 hours. Virus-containing supernatant was collected at 48 and 72 hours post-transfection.

HEK 293T cells were transduced by spin infection using the above lentivirus and 6µg/ml polybrene and transduced clones were selected using 14µg/ml blasticidine for 48 hours. Stably transduced cells were maintained in DMEM (Thermo #11960044), 10% FCS, pen/strep and sodium pyruvate. Transduced cells were periodically re-selected with 14µg/ml blasticidine for at least 48 hours.

Flow cytometry

Mouse

N2a cells stably expressing full-length V5-tagged mFIBCD1, mFIBCD1 lacking the fibrinogen domain (Δ FReD) or the empty vector (pMSCV-IRES-mCherry) were washed once with PBS and incubated for 4 hours with 100µg/ml fluoresceinamine labelled glycosaminoglycans: 4-O-sulfated chondroitin sulphate (AMS.CSR-FACS-A1, AMSBIO), poly-sulphated chondroitin sulphate (AMS.CSR-FACS-P1, AMSBIO) or dermatan sulphate (AMS.CSR-FADS-B1, AMSBIO) in DMEM. See Supplementary Table 2 for a list of flow cytometry antibodies used in this study. The staining medium was removed, cells were collected by gentle flushing with PBS and fluorescence was measured by FACS LSR Fortessa (BD). The experiment was performed in three independent replicates and analysed by FlowJo v10.6 (FlowJo LLC).

Human

Untransduced HEK 293T cells or those stably expressing full length C-terminally 3xFLAG tagged hFIBCD1, hFIBCD1_W6*, hFIBCD1_G29S, hFIBCD1_R406C, hFIBCD1_P456L were seeded in full media. The next day, cells were washed 1x with PBS and trypsinised for precisely 1.5 minutes, pelleted at 4°C, and resuspended in 10µg/ml 4-O-sulfated chondroitin sulphate (AMS.CSR-FACS-A1, Amsbio) diluted in freshly prepared PBS (0.8mM CaCl₂) and incubated in a humidified incubator for 45 minutes. The cells were washed 1x in ice-cold PBS (0.8mM CaCl₂) and acquired on a LSRFortessa Cell Analyzer (BD Biosciences). The experiment was performed in two independent replicates and analysed by FlowJo v10.6.1 (FlowJo LLC).

Protein isolation, Immunoprecipitations, and Western blots

For protein extraction, hippocampi tissues were manually homogenized in 300 µl ChABC buffer (40 mM Tris-HCl pH 8.0, 40 mM sodium acetate, C3667, Sigma) containing Benzonase supplemented with Halt protease/phosphatase inhibitor cocktail (Thermo Scientific). After 10 minutes full-speed centrifugation, the supernatant containing the soluble protein fraction was separated from the pellet (insoluble fraction), which was resuspended in 300 µl ChABC buffer. Two aliquots of each fraction were brought to a protein concentration of 3 µg/µl (75µg protein in 25 µl ChABC buffer) and one aliquot of each fraction was further incubated with ChABC for 12 hours at 37°C. After adding 25 µl of Lämmli buffer, samples were heated 5 minutes at 95°C and 30µl were separated by SDS-PAGE and transferred onto PVDF membranes (Immobilion-P, Merck Millipore) according to standard protocols. Blots were blocked for 1 hour with 5% milk in TBST (1x TBS and 0.1% Tween-20) and were then incubated overnight at 4°C with primary antibodies (1:100, anti CS-0S, 1B5; anti CS-4S, 2B6, antiCs-6S, 3B3; amsbio) diluted in 5% milk in TBST. Blots were washed 3 times in TBST for 5 minutes and were then incubated with HRP-conjugated secondary anti-mouse-IgG-H&L chain (Promega)

or anti-rabbit-IgG-F(ab')₂ (GE Healthcare) antibody for 1 hour at room temperature, washed 3 times in TBST for 5 minutes and visualized using enhanced chemiluminescence (ECL, GE Healthcare). See Supplementary Table 2 for a list of antibodies used in this study. β -Actin was used to control for protein loading.

Immunoprecipitation

N2a cells expressing FIBCD1, FIBCD1 Δ FR_{ED} or empty vector were washed twice with PBS and lysed in Hunt buffer (20 mM Tris-HCl pH 8.0, 100 mM sodium chloride, 1 mM EDTA, 0.5% NP-40) supplemented with Halt protease/phosphatase inhibitor cocktail (Thermo Scientific) in 3 consecutive freeze and thaw steps. After full-speed centrifugation, the supernatant containing the soluble protein fraction was further used. An equal amount (500 μ g) of each protein lysate was precleared for 1 hour with magnetic Protein G Dynabeads (Invitrogen) and immunopurified with 40 μ l washed anti-V5 agarose beads (Sigma) overnight at 4°C. After 5 washing steps in Hunt buffer, input (1/16 of the immunoprecipitation corresponding to 30 μ g) and immunoprecipitation samples were separated by SDS-PAGE, blotted and stained with an antibody against V5 (ab15828, 1:2000 dilution), and Western blotting was performed as described above.

Immunofluorescence/IHC

Primary Neurons

At 2 or 14 days after plating (DIV2 and DIV14, respectively), primary neuronal cultures were washed with PBS and then fixed in 4% PFA with 4% glucose for 10 minutes at room temperature, and subsequently quenched with 10 μ M glycine/PBS for 10 minutes at room temperature. They were then washed twice with 0.01% Triton-X/PBS (PBST), permeabilized with 0.25% Triton-X/PBS for 3 minutes and blocked in 5% NGS for 1 hour. Primary antibodies were incubated overnight at 4°C and washed 3 times in PBST. Secondary antibodies were

incubated for 1 hour at room temperature and washed 3 times with PBST before mounting in ProLong Gold Antifade Mountant (Thermo #P10144). Images were acquired on fluorescent microscope (Leica), acquiring semi-random fields of the coverslips. Images were analysed manually using ImageJ. Experimenters were blinded to genotype and plating conditions during image analysis.

Drosophila melanogaster

Wandering third instar female larvae were dissected in Ca⁺ free PBS and fixed in 4% paraformaldehyde for 20 minutes. Larval body walls were blocked in serum, then incubated in primary antibodies overnight and secondary antibodies at room temperature for 2 hours while rocking. Samples were mounted in Prolong Diamond (Invitrogen) for analysis using the Zeiss LSM780 confocal microscope. Bouton number and axon branching were all identified using the anti-HRP antibody using ImageJ (NIH).

HEK 293T cells

Untransduced HEK 293T cells and HEK 293T cells stably expressing full length 3xFLAG tagged (C-terminal) hFIBCD1, hFIBCD1_W6*, hFIBCD1_G29S, hFIBCD1_R406C, hFIBCD1_P456L were seeded onto glass coverslips. The next day, the cells were rinsed 1x with PBS and fixed in 4% PFA (supplemented with 4% glucose) for 10 minutes at room temperature, then quenched for 10 minutes with PBS (0.01M glycine) for another 10 minutes at room temperature. The cells were washed 2x with PBS then permeabilised with 0.25% Triton-X PBS for 1.5 minutes, washed 1x with PBS and blocked for 1 hour with 5% normal goat serum at room temperature. Primary antibodies (anti-FLAG, 1:1000) were added overnight at 4°C, washed 2x with PBS, then secondary antibodies added (Alexa Fluor Anti-mouse 546, 1:500) and DAPI (1:2000) incubated at room temperature for 1 hour, washed again 2x with

PBS then mounted in ProLong Gold Antifade mounting media and imaged on a Zeiss LSM980 confocal microscope.

MRI imaging

Anaesthetised male C57Bl6/J mice (12 month of age) and their *Fibcd1* KO littermates were imaged in the Preclinical Imaging Facility at Vienna Biocentre Core Facilities (pcPHENO, VBCF), member of Vienna Biocentre (VBC), Austria, as described previously⁷². Briefly, a 15.2 Tesla MRI (Brucker BioSpec, Ettlingen Germany) was used to image brains of anaesthetised animals (isoflurane 4% induction, maintenance with 1.5%, Vana GmbH) with a 3D fast long angle shot (FLASH) sequence with magnetization transfer pulse. Each 3D image set was manually segmented using Amira 5.6 (Visualization Science Group) using The Paxinos mouse brain atlas as a reference⁷³. Values were normalized to brain size, averaged and presented as percentage of total brain volume.

PNN visualisation with WFA

Brain was dissected from 8-10 week-old *Fibcd1* WT and KO mice and fixed in 4% paraformaldehyde and paraffin-embedded followed by 20µm coronal sectioning. For staining, the tissues were re-hydrated with PBS, permeabilized in 0.5% Triton-X PBS for 15 mins at room temperature (RT) followed by blocking in 10% goat serum diluted in 0.25% Triton-X PBS for 1 hour at RT. After 2x 3 mins washes with 0.1% tween-20 PBS, endogenous IgGs were blocked using goat F(ab) anti-mouse IgG (1:2000) diluted in 0.1% tween-20 PBS for 1 hour at RT. Next, tissues were washed 3x 3mins in 0.1% tween-20 PBS. Fluorescein *Wisteria Floribunda* Lectin (FL-1351, 1:500, Vector Laboratories) was diluted 1:500 in 0.1% tween-20 PBS with 2% goat serum and DAPI (Roth #6335, 1:2000) for 1 hour at RT. Tissues were washed 3x 3mins in 0.1% tween-20 PBS and mounted using Fluoromount Aqueous Mounting Medium (Sigma #F4680). Images were acquired using Vectra Polaris (Akoya).

Tissue sGAG quantification

11-13-week-old *Fibcd1* WT and KO mice (mix of male and female) were sacrificed by CO₂ asphyxiation and the hippocampi dissected out and snap frozen in liquid nitrogen. Samples were weighed and analysed for sulphated GAG (sGAG) amounts using Blyscan Glycosaminoglycan Assay kit (Biocolor #B1000), following the manufacturer's instructions, including Papain extraction (Sigma #P3125).

HPLC

Chondroitin sulphate was extracted from defatted, pronase digested mouse microdissected hippocampi (CA1 region) and digested using Chondroitinase ABC (from *Proteus vulgaris*, Sigma-Aldrich #C3667). The resulting glycosaminoglycan-disaccharides were fluorescently labelled with 2-aminobenzamide by reductive amination and were analysed according to previous literature⁷⁴. Identity of glycosaminoglycan-derived disaccharides was inferred from retention time alignment with the major constituents of chondroitin sulphate sodium salt from shark cartilage (Sigma-Aldrich, C4384), and bovine trachea (Sigma-Aldrich #C9819).

Behaviour assays

Mouse

Elevated Plus Maze were performed as described previously using an automated activity system (TSE-Systems, Germany)⁷². Mice were trained in the Morris Water Maze (pcPHENO, VBCF) as described previously⁷². T-Maze was performed as described previously⁷².

Drosophila negative geotaxis assay

Female *Nsyb-Gal4* animals were crossed with the *UAS-RNAi* lines targeting *CG10359*. Female offspring were tested at 10d after eclosion. Offspring were flipped every third day and no more than 10 flies were kept in each vial. Flies were knocked-out with CO₂, sorted into batches of 3-

7 and given 25h to recover before testing. On the day of testing, flies were flipped into empty vials and given 10-15m to recover. The climbing index is the percentage of flies that pass the 5cm mark in 5s after gently tapping to the bottom of a plastic vial.

Acute hippocampal slice preparation and electrophysiological recordings

Memory-related synaptic plasticity and electrophysiological recordings were studied *ex vivo* in hippocampal slices essentially as previously described⁷⁵⁻⁸⁰. Briefly, mice were sacrificed by rapid cervical dislocation and swift sharp-blade decapitation. Brains were rapidly extracted and immediately immersed in a frosty artificial cerebrospinal fluid solution (aCSF) containing (in mM): 125 NaCl, 2.5 KCl, 25 NaHCO₃, 2 CaCl₂, 1 MgCl₂, 25 D-glucose, and 1.25 NaH₂PO₄ (all from Sigma-Aldrich). In all experimental conditions, aCSF was continuously bubbled with a mixture of 95% oxygen and 5% carbon dioxide (Carbogen). Hippocampi were dissected while submerged in aCSF and transverse slices (300 µm in thickness) were obtained using a McIlwain Tissue Chopper (Mickle Laboratory Engineering, UK). Slices were quickly transferred to a custom-built submerged recovery chamber, where they rested for at least 1 hour submerged in 100 ml of aCSF maintained at 30 ± 2 °C. For enzymatic treatments, slices were transferred to independent home-made digestion chambers containing 15 mL of aCSF (with 0.1% bovine serum albumin) plus 0.2U/mL of either Penicillinase (Pen) (Sigma-Aldrich #61305) or *Proteus vulgaris* Chondroitinase-ABC (ChABC) (Sigma-Aldrich#C3667). Slices were enzymatically treated for 2 hours at 37°C. After enzymatic treatment, slices were rinsed in separated beakers containing 100 mL of aCSF (32 ± 1 °C) and gently transferred back to their corresponding recovery chamber for subsequent electrophysiological analysis. The synaptic function was studied by examining the electrical properties of the CA3-Schaffer collateral to CA1 circuit. The CA3-CA1 Schaffer collateral pathway was stimulated electrically via a home-made bipolar tungsten electrode insulated to the tip (50 µm tip diameter) and using an ISO-STIM 01D isolator stimulator (NPI Electronics, Tamm, Germany). Evoked field excitatory postsynaptic

potentials (fEPSPs) were recorded at the CA1 area using aCSF-filled glass micropipettes (2–4 M Ω) located about 400 μ m away from the stimulating electrode. Input/output curves were obtained by delivering increasing pulses of voltage (100 μ s in duration) between 0–9 V with a delta of 1 V and 10 s between pulses. The strength of synaptic transmission was determined in each case from the decaying slope of recorded fEPSPs. To examine paired-pulse-induced synaptic facilitation, two pulses of voltage with a strength eliciting 40% of the maximum inducible fEPSPs amplitude as determined by input/output measurements (40% fEPSP_{max}) were delivered at variable inter-pulse intervals ranging between 20–100 ms with a delta increment of 20 ms (pulse pairs delivered every 10 s). The decaying slopes of the evoked fEPSPs for each consecutive pair of pulses was measured and the strength of synaptic potentiation was determined from the 2nd/1st fEPSPs slope ratio. To study long-term potentiation, basal synaptic transmission (baseline) was examined for at least 20 min by recording stable fEPSPs in response to 40% fEPSP_{max} stimulating voltage pulses (100 μ s duration; fEPSPs elicited at 0.03 Hz). After recording a steady baseline, a theta-burst stimulation (TBS) protocol was applied, consisting of five trains of 40% fEPSP_{max} stimulating voltage pulses at 100 Hz (100 μ s/pulse, with 4 s inter-train interval). Postsynaptic signal in response to baseline stimulating conditions was measured for 35–70 min as indicated in figure legends. Synaptic potentiation was determined by examining the temporal course of the decaying fEPSPs slopes following TBS, normalized to baseline values. Data from fEPSPs slopes attained when measuring long term potentiation were averaged for every 2 minutes. All recordings were made using an AxoClamp-2B amplifier (Bridge mode) and a Digidata-1440 interface (Axon Instruments). Data (5–22 slices/condition) were analysed using the pClamp-10 Program software (CA/Molecular Devices, USA).

Sequence alignment

Human and mouse Fibcd1 and Drosophila CG10359 ‘Fibrinogen C-terminal’ protein sequences were acquired from Uniprot.org. Multiple sequence alignment (MSA) was done using ClustalO algorithm (<https://www.ebi.ac.uk/Tools/msa/clustalo/>)⁸¹.

Statistical analysis

Flow cytometry

Samples analysed by 1-way ANOVA.

Immunofluorescence

Images were counted manually and analysed by 1-way ANOVA. Experimenters were blinded to genotype and condition during analysis.

Mouse behaviour

Data was analysed by unpaired Student’s t-test. n= an individual mouse.

Drosophila

All data sets were organized and analysed in Microsoft Excel and Prism. Statistical test type listed in the figure legends. Data sets with equal variance were analysed using ANOVA and Dunnett’s post-hoc analysis for multiple comparison. Significance is defined as $P < 0.05$ and error bars are shown as standard error of the mean (SEM) unless otherwise noted.

Electrophysiology

Two-way ANOVA with repeated measures was used to compare values between treatment groups for input/output, paired-pulse and LTP set of data as depicted in scatter charts comparing pairs of values. Two-way ANOVA was used to compare values between treatment groups at a single time or voltage point as depicted in bar charts. Data values are represented as mean \pm S.E.M. (p values < 0.05 were considered statistically significant). * $p \leq 0.05$; ** $p \leq 0.01$; *** $p \leq 0.001$; **** $p \leq 0.0001$

914 Table of oligonucleotide sequences

Genotyping primers:

<i>Fibcd1</i> WT	CGCTGGTCTTGCTGGAAG TCTTCTCTTCCCTCTGCACA
<i>Fibcd1</i> KO	GCAGCGCATCGCCTTCTATC TGGCACAGGTTAAGGAATT

Primers for qPCR:

<i>Gapdh</i>	GTCGGTGTGAACGGATTTGG GACTCCACGACATACTCAGC
<i>mFibcd1(ex1-2)</i>	CTGGAAGATGGTCCACGAG CCGTGCACAGGACATAACTG
<i>mFibcd1(ex3-4)</i>	TCAAGGCTGACCTTCAGAGG GAAGCCAGCTGGGTAGTGAG
<i>mFibcd1(ex4-5)</i>	CAGCTGGCTTCCAGGTCTAC CCAACCTCGGAAAAAGTTCA
<i>hFibcd1</i>	CAGGACGATGGCGTCTACTC GATCCTCTTGAGCCCTAGCC

915

916 Table of additional materials

<u>Antibodies for immunoblots:</u>	
β -Actin	A5316 (Sigma)
CS-0S (1B5)	270431-CS (Amsbio)
CS-4S (2B6)	270432-CS (Amsbio)
CS-6S (3B3)	270433-CS (Amsbio)
Anti-V5 tag	Ab15828 (Abcam)
<u>Fluorescent Sugars for Flow Cytometry:</u>	
Fluoresceinamine Labeled Sodium Chondroitin Sulfate A (A1)	AMS.CSR-FACS-A1 (Amsbio)
Fluoresceinamine Labeled Sodium Chondroitin Poly-Sulfate (P1)	AMS.CSR-FACS-P1 (Amsbio)
Fluoresceinamine Labeled Sodium Dermatan Sulfate (B1)	AMS.CSR-FADS-B1 (Amsbio)
<u>Antibodies/dyes for immunofluorescence:</u>	
MAP2	Millipore 05-346
FLAG (M2)	Sigma F1804
Alexa Fluor® 546 anti-mouse	Thermo A-11003
Goat F(ab) anti mouse (IgG)	Abcam (ab6668)
Alexa Fluor® 647 AffiniPure Goat Anti-Horseradish Peroxidase	Jackson Immunoresearch
Mouse anti-nc82 (Bruchpilot)	Developmental Hybridoma Studies Bank
DAPI	Carl Roth
WFA-488	Vector Laboratories (FL-1351)

917

918 Table of Drosophila Reagents

<u>Drosophila reagents</u>	
----------------------------	--

<u>Stock</u>	<u>RRID/source</u>
y[1] w[*]; P{w [+mC]=r4-GAL4}3	BDSC_33832
y[1] v[1]; P{y[+t7.7] v[+t1.8]=TRiP.HMJ30271}attP40	BDSC_63703
w1118; P{GD2280}v4128/TM3	FlyBase_FBst0464025
P{KK105143}VIE-260B	FlyBase_FBst0474536
y[1] w[*]; P{w[+m*]=nSyb-GAL4.S}3	BDSC_51635
y[1] w[*]; P{w[+mC]=tubP-GAL4}LL7/TM3, Sb[1] Ser[1]	BDSC_5138
PBac{UAS-empty}VK00037	Yoon et al., Cell Metabolism, 2017
y[1] v[1]; P{TRiP.JF01355}attP2	BDSC_31603

919

920

		Patient 1	Patient 2
Background	Sex	M	F
	Current Age	12 y.o.	3 y.o.
	Ethnicity	Caucasian	Chinese
	Karyogram	46, XY	46, XX
	Consanguinity	No	No
	FIBCD1 Variant	Compound Het. Chr9:133805421 C>T; Chr9:133779621 G>A c.85G>A ; c.1216C>T p.G29S ; p.R406C	Homozygous Chr9:133779470 G>A c.1367C>T p.P456L
	Family Segregation	AR	UPD with mosaicism
	Other Variants	n/a	UNC13B (p.C511R) and RIC1 (p.A984V)
Neurology	Diagnosis	Severe ASD	Severe NDD
	Psychological Evaluation	Delayed social abilities	Delayed social abilities
		Poor eye contact	
		Borderline delayed cognition	Delayed cognitive abilities
		Anxiety	
		ADHD combined type	
	Sitting and Walking	Normal	Delayed
	Language	Nonverbal	Nonverbal
	Epilepsy	-	-
	Intellectual Disability	-	Too young to be evaluated
	Sensory	High pain tolerance, sensitive touch	n/a
	Motoric	Fine motor coordination deficits	n/a
Neuroradiology	MRI	n/a	Slightly thickened cortex
			Decreased white matter volume
			Ventriculomegaly
			Bilateral enlarged frontal gyri
			Microcephaly
Dysmorphias	Craniofacial	Triangular shaped head	Micrognathia
		Hypertelorism	
		Almond-shaped eyes	
		Posteriorly rotated and low set ears	Low set ears
		Epicanthal folds	
Other Systems	Cardiovascular	-	Patent ductus arteriosus, resolved at 6 months
	Respiratory	-	Recurrent pneumonia
	Immune	Allergic rhinitis, sinusitis	-

921 **Table 1:** Summary of patient clinical findings.

Figure 1:

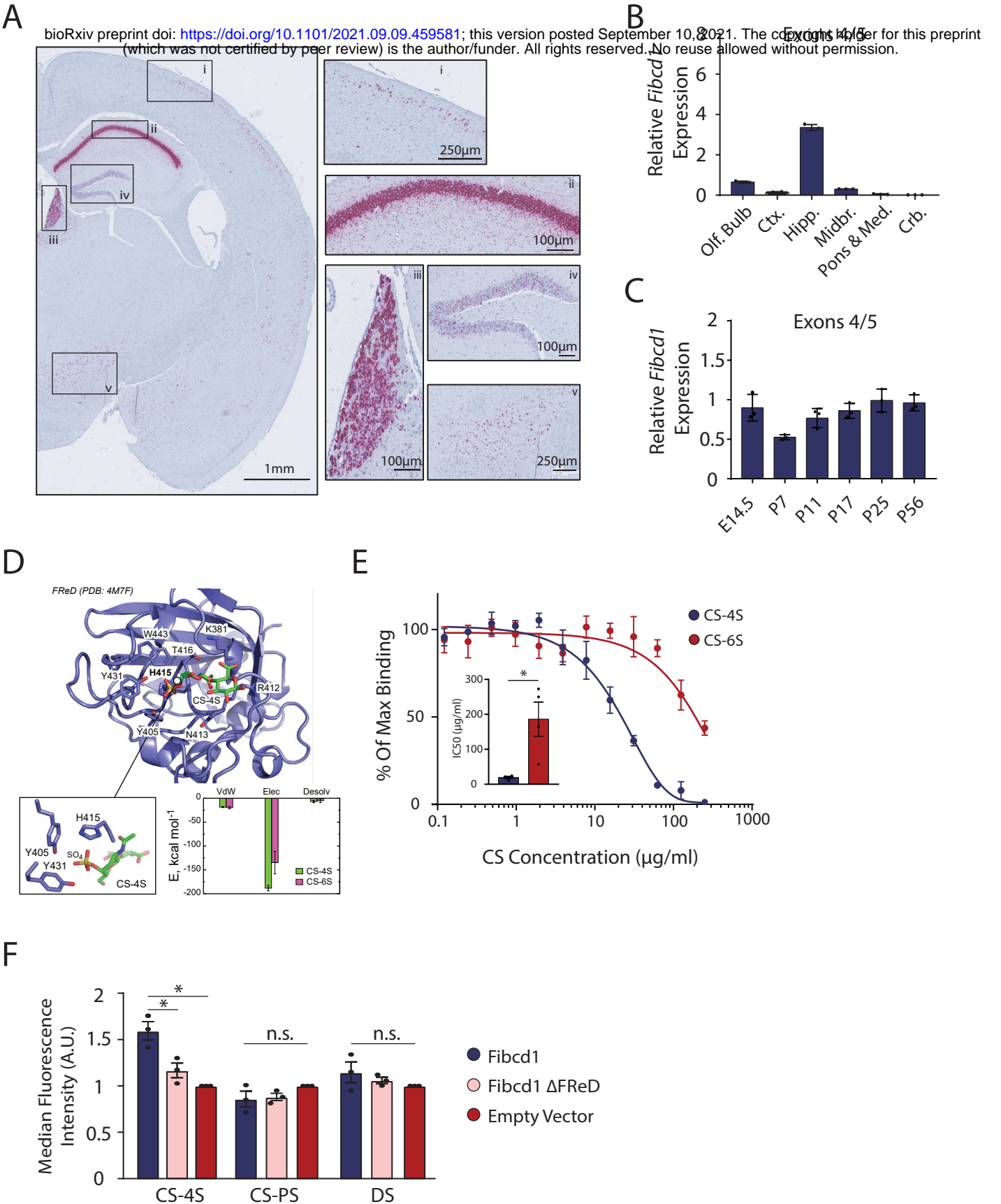


Figure 2:

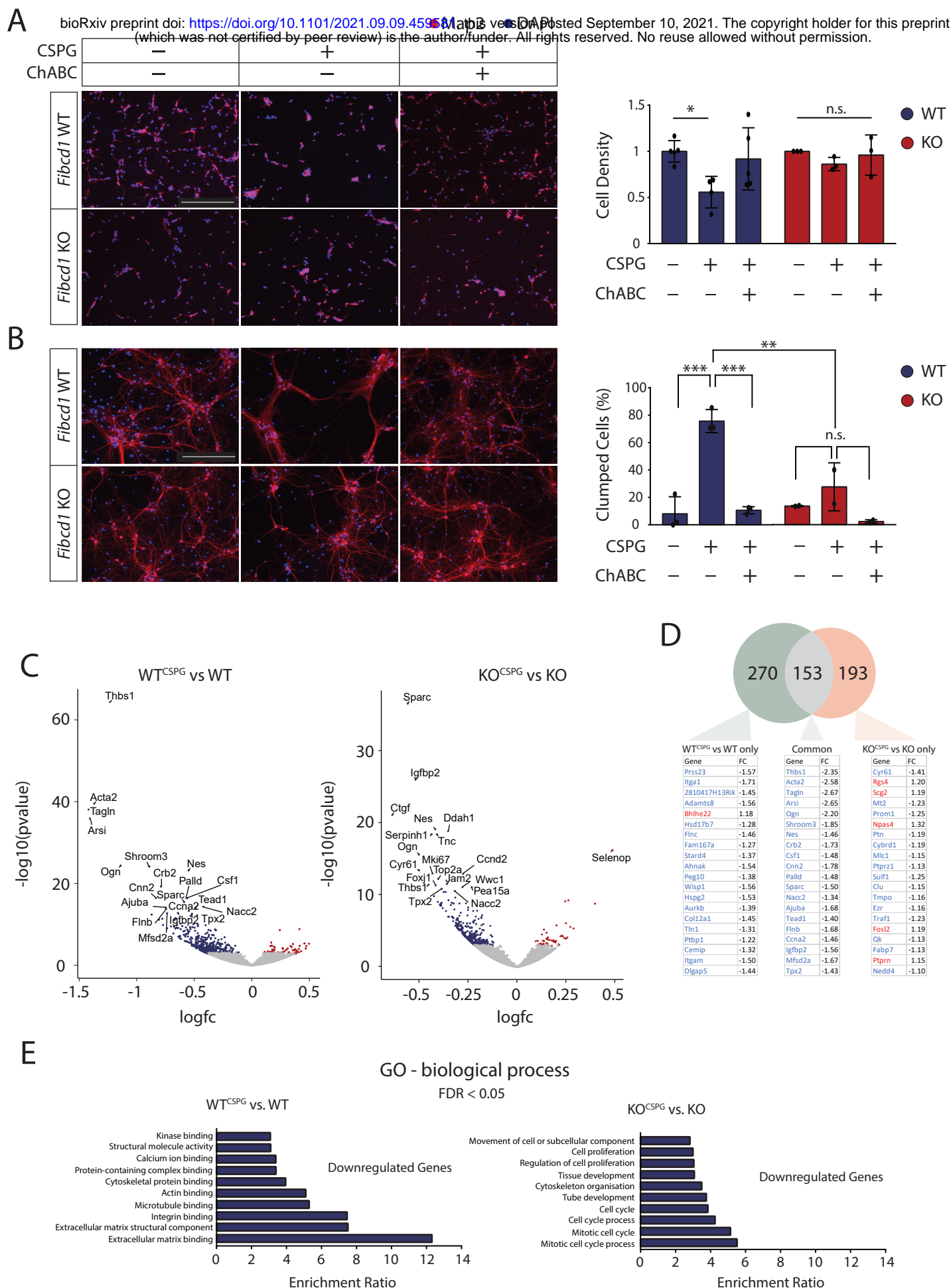


Figure 3:

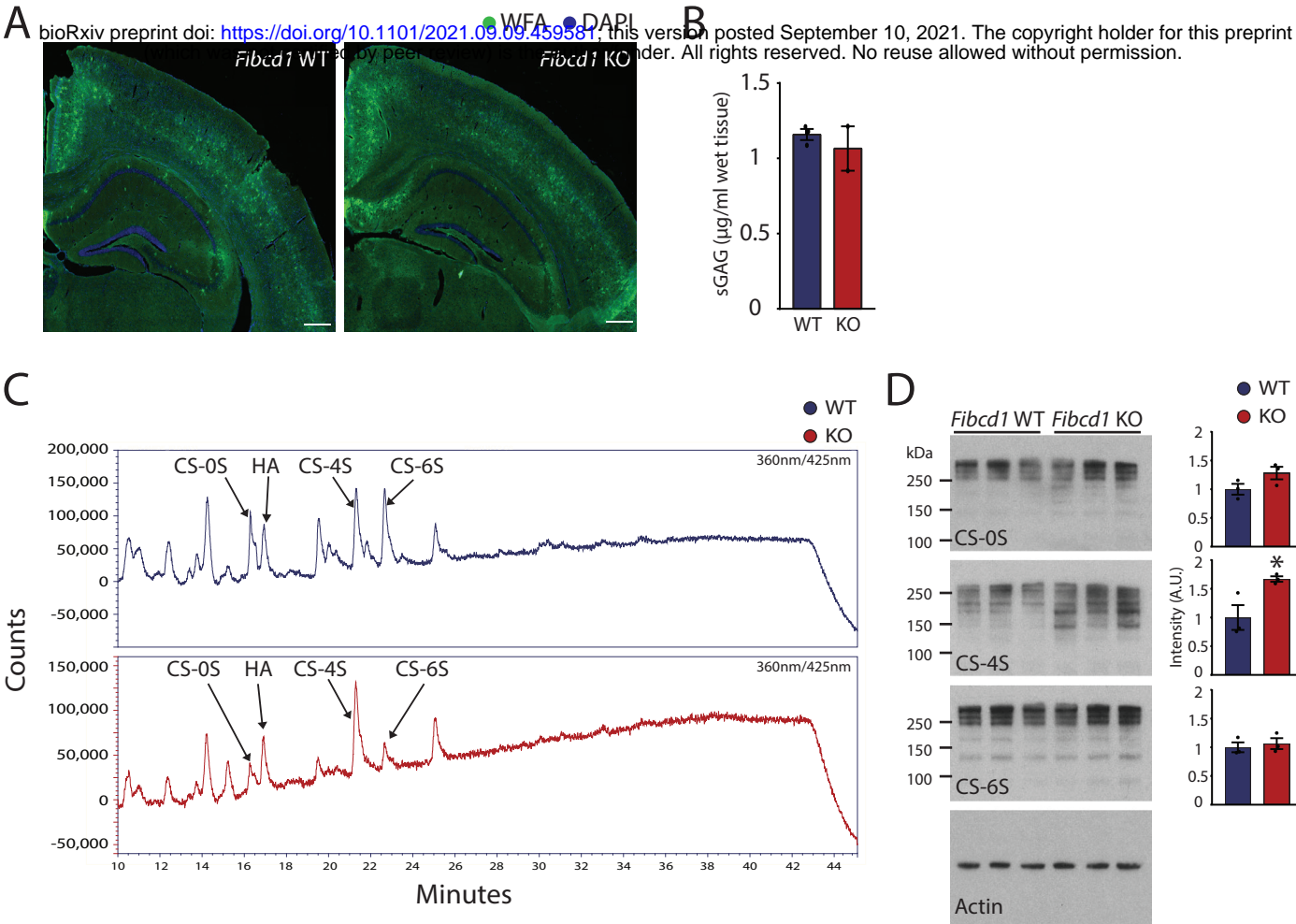


Figure 4

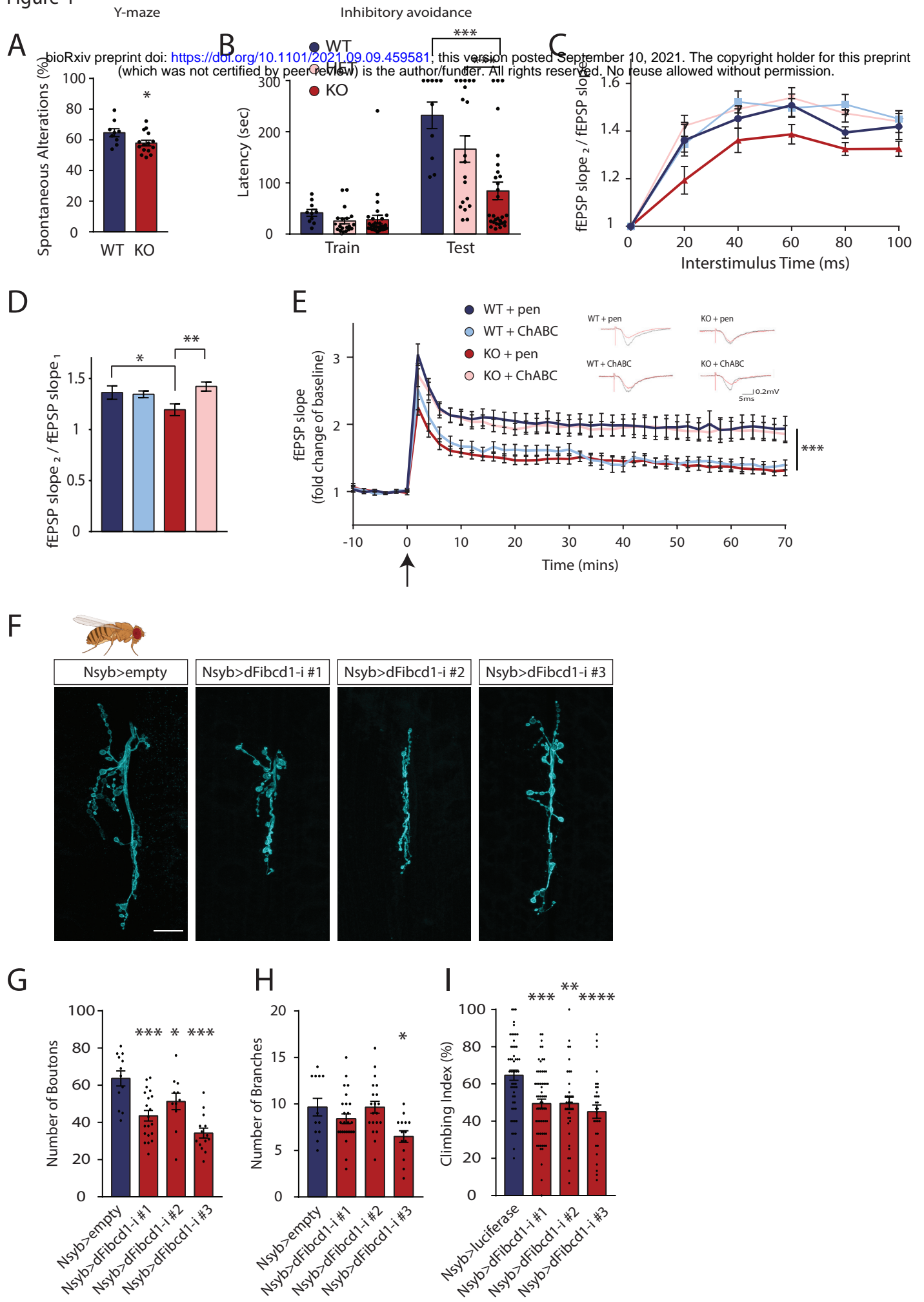


Figure 5

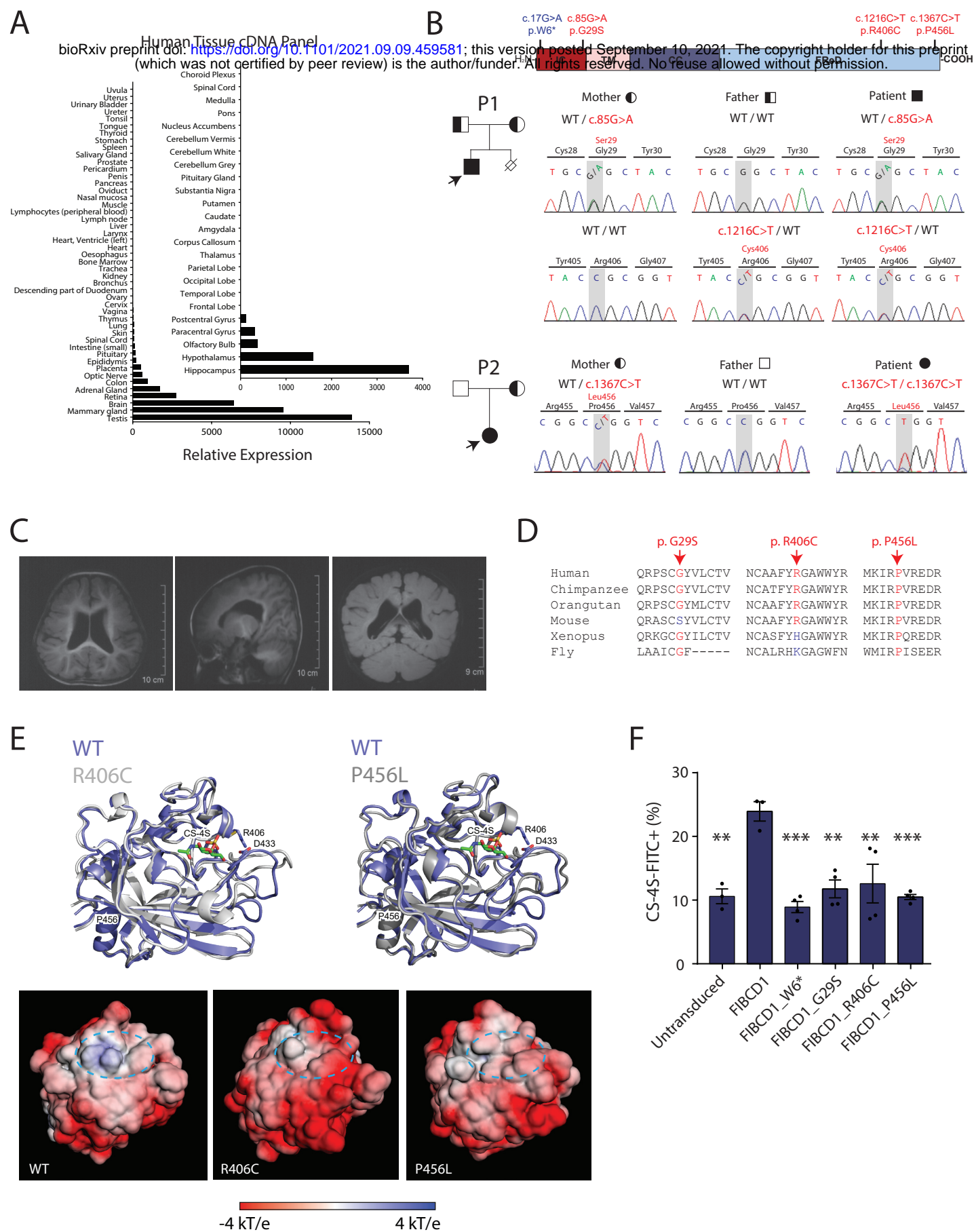


FIGURE TITLES AND LEGENDS

Figure 1: ***Fibcd1* is expressed in the adult and developing mouse brain in discrete regions.**

(A) In-situ hybridisation with probe pairs specific to *Fibcd1* mRNA (purple) in mouse whole-brain coronal section, left hemisphere shown. Insets of high *Fibcd1* expressing regions are (i) cortex, (ii) pyramidal cell layer of hippocampus, (iii) medial habenula, (iv) granule cell layer of the dentate gyrus and (v) hypothalamus. Scale bar sizes are as indicated. Representative of 3 independent experiments. (B) Relative mRNA expression levels of *Fibcd1* (primers binding to exon 4 and 5) normalised to *Gapdh*, in the indicated adult mouse brain regions, analysed by RT-qPCR (n = 3). Olf.Bulb = olfactory bulb; Ctx. = cortex; Hipp. = hippocampus; Midbr. = midbrain; Pons & Med = pons and medulla; Crb. = cerebellum. (C) Relative mRNA expression levels of *Fibcd1* (primers binding to exon 4 and 5) normalised to *Gapdh* in the hippocampus of the indicated developmental time points, analysed by RT-qPCR (n = 3). Data is represented as mean and error bars represent SD. (D) Top binding pose for *in silico* docking of CS-4S to FIBCD1 FReD (PDB 4M7F). Inset (left) is the orientation of CS-4S within the FReD binding pocket and (right) binding free energy of CS-4S vs CS-6S. Van der Waals (vdW), electrostatic (Elec) and desolvation (Desolv) components of binding free energy charge. (E) Competitive ELISA with increasing concentrations of CS-4S (blue circles) or -6S (red circles) incubated with recombinant FIBCD1 FReD and immobilised acetylated BSA. Inset is IC50 concentrations for CS-4S and CS-6S. Data is represented as mean and error bars represent SEM. (F) Flow cytometric analysis of N2a cells expressing full-length mFIBCD1, mFIBCD1ΔFReD or empty vector control incubated with FITC-tagged chondroitin-4-sulfate (CS-4S), polysulphated chondroitin sulphate (CS-PS) or dermatan sulphate (DS) (N = 3). Error bars represent SEM. * = p ≤ 0.05.

Figure 2: FIBCD1 mediates responses of primary hippocampal cultures to CSPGs.

(A) Left, Representative images of immunofluorescent staining (MAP2, red; DAPI, blue) of primary hippocampal cultures at 2 days *in vitro* (DIV), plated on +/- CSPG coating with and without prior digestion with ChABC, as indicated. Right, quantification of DIV2 images, showing the number of protruding cells per field normalised to untreated condition. N(WT) = 3; N(KO) = 2. (B) Left, representative images of DIV14 neurons, same conditions as (A). Right, quantification of DIV14 images, representing the percentage of clumped cells per field. N(WT) = 3; N(KO) = 2. Error bars represent SD. * = $p \leq 0.05$; ** = $p \leq 0.01$; *** = $p \leq 0.001$. Scale bar = 250 μ m. (C) Volcano plots of differential gene expression of transcriptomes at DIV2 hippocampal cultures comparing (left) WT^{CSPG} vs WT and KO^{CSPG} vs KO (FDR < 0.05) (right). Significantly upregulated and downregulated genes are shown in red and blue, respectively. The top 20 differentially expressed genes are labelled. (D) Above, Venn diagram of significant DEGs unique to WT^{CSPG} vs WT (green, 270 genes), KO^{CSPG} vs KO (orange, 193 genes) and common between the two (grey, 153 genes). Below, lists of the 20 most significant DEGs and their fold change for each comparison, showing downregulated DEGs in blue and upregulated in red. (E) GO term enrichment analysis for significantly downregulated genes (FDR < 0.05) in (left) WT^{CSPG} vs WT and (right) KO^{CSPG} vs KO.

Figure 3: *Fibcd1* KO hippocampi have accumulated CS-4S compared to WT littermates.

(A) Representative images of WFA-staining of PNNs in a coronal section of *Fibcd1* WT (left) and KO (right) mouse brains, left hemisphere (WFA, green; DAPI, blue) Scale bar = 400 μ m. (B) Quantification of sulphated GAG amount (per mg of wet tissue) in dissected 11-13 week old *Fibcd1* WT and KO hippocampi. Error bars represent SD. (C) HPLC traces (representative of 3 independent experiments) of variously sulphated GAGs (as labelled) in adult *Fibcd1* WT

(top, blue) and KO (bottom, red) CA1 pyramidal cell layer hippocampi. Unsulphated CS = CS-0S; hyaluronic acid = HA; carbon 4 sulphated CS = CS-4S; carbon 6 sulphated CS = CS-6S. (D) Immunoblot analysis (left) and quantification of signal intensity (right) of littermate WT (blue) versus *Fibcd1* KO (red) adult hippocampi with antibodies against CS-0S, CS-4S, CS-6S and actin as a loading control. Each lane represents an independent animal (n = 3). Protein marker sizes are indicated. Error bars represent SEM. * $p \leq 0.05$.

Figure 4: Neurological deficits in FIBCD1 deficient mice and flies.

(A) Percentage of spontaneous alterations in the Y-maze. N(WT) = 9; N(KO) = 15. (B) Latency to enter the dark (foot shock) chamber during the inhibitory avoidance task at training and testing (24 hours post-training) periods. *Fibcd1* WT, heterozygous (HET) and KO mice shown. N(WT) = 8; N(HET) = 19; N(KO) = 15. Error bar represent SEM. (C-D) Paired-pulse facilitation in CA3-CA1 Schaffer collateral pathway of acute hippocampal slices from *Fibcd1* WT and KO mice. Pre-treatment with enzymes penicillinase (+pen) or Chondroitinase ABC (+ChABC) is indicated. N (WT+pen) = 17; N (KO+pen) = 20; N (WT+ChABC) = 19; N (KO+ChABC) = 25. (E) Long-term potentiation in CA3-CA1 Schaffer collateral pathways of acute hippocampal slices. Theta burst stimulation (TBS) is at time 0 indicated by the arrow. N (WT+pen) = 9; N (KO+pen) = 15; N (WT+ChABC) = 6; N (KO+ChABC) = 12. Inset are representative traces. (F) Immunofluorescent images (representative of 3 independent experiments) of control and neuronal (Nsyb) *CG10359* (*dFibcd1*) RNAi-mediated knockdown *D. melanogaster*, 3rd instar larvae NMJ (NMJ6/7) stained with anti-horseradish peroxidase antibody. Empty control and RNAi-mediated knockdown of *CG10359* (*dFibcd1-i*) lines 1, 2 and 3 shown. Scale bar = 20µm. (G) Quantification of (F), control and *CG10359* knockdown lines NMJ neuron bouton number. (H) Quantification of (F), control and *CG10359* knockdown lines NMJ neuron axon branch points. (E) Negative geotaxis assay of adult *Drosophila* control

and RNAi lines #1, #2 and #3 compared to control lines expressing RNAi targeting luciferase.

Climbing index represent the percentage of flies that crossed the 5 cm vial mark within 5 seconds after gentle tapping to the bottom of the vial. n is the number of tested vials. N (luciferase) = 53; N (line #1) = 63; N (line #2) = 36; N (line #3) = 31. For flies per vial, see Figure S6C). * = $p \leq 0.05$; ** = $p \leq 0.01$; *** = $p \leq 0.001$. Error bars represent SEM.

Figure 5: Expression of *FIBCD1* in human tissues and properties of *FIBCD1* variants identified in 2 cases of undiagnosed neurodevelopmental disorders.

(A) *Fibcd1* expression in various human visceral tissues and (inset) brain regions. Expression is plotted relative to the tissue with lowest detectable expression (trachea; inset, choroid plexus) (B) Top, schematic of FIBCD1 protein, with labelled intracellular domain (IC, red), transmembrane domain (TM, pink), coiled coil (CC, dark blue) and FReD in dark blue. Location of patient variants denoted in red, and of control in blue. Family pedigrees of P1 (top) and P2 (bottom) showing affected proband (filled, arrow) and carriers (half-filled, arrow). Right, representative traces of Sanger sequencing to confirm segregation within the family. P1 variants are inherited in autosomal recessive manner; P2 exhibits inheritance by uniparental disomy. Above, schematic of FIBCD1 with location of patient variants and p.W6* indicated. (C) P2 MRI images (axial, coronal and sagittal plane) showing ventriculomegaly, slightly thickened cortex and bilateral enlarged gyri. (D) Amino acid sequence conservation sites of patient variants Gly29Ser, Arg406Cys and Pro456Leu in various species. (E) Top, ribbon diagrams of the superposition of the WT FReD domain with R406C (left) and P456L (right) mutants. The loops surrounding the ligand binding site (389-399 and 423-448) exhibit the largest structural rearrangement in both mutants. Bottom, comparison of the electrostatic potential mapped onto the solvent-accessible surface between WT and the two variant FReDs. (F) Flow cytometric analysis of untransduced HEK293T cells, or expressing constructs with

1027 full-length wild-type human FIBCD1, FIBCD1 with the W6* early stop variant as control

1028 (FIBCD1_W6*), or the three patient variants incubated with FITC-tagged CS-4S represented

1029 as percentage of CS-4S-FITC relative to unstained control. Statistics were calculated by 1-way

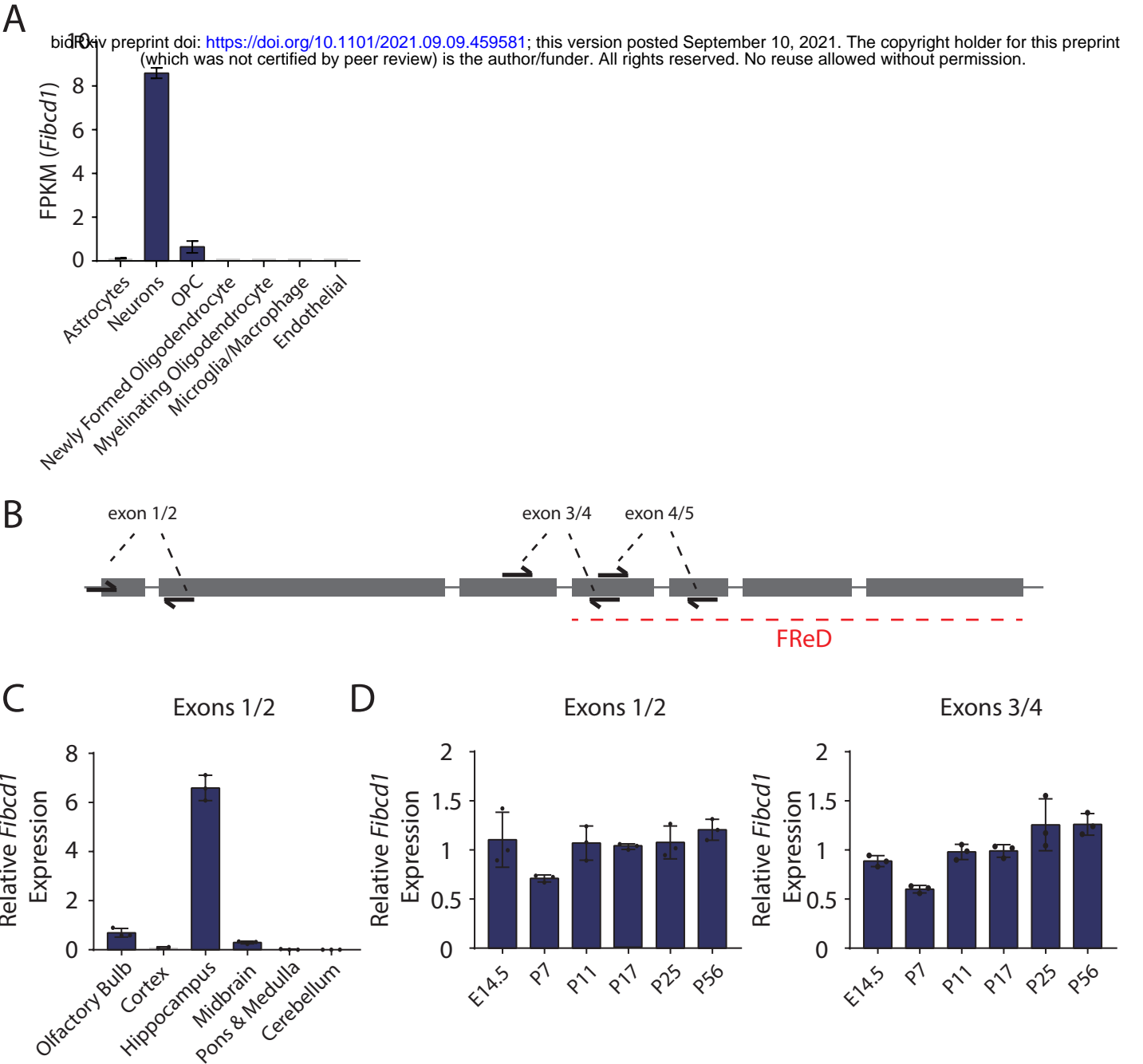
1030 ANOVA, comparing to the FIBCD1 condition. ** = < 0.01; *** = < 0.01; **** = <0.001.

1031

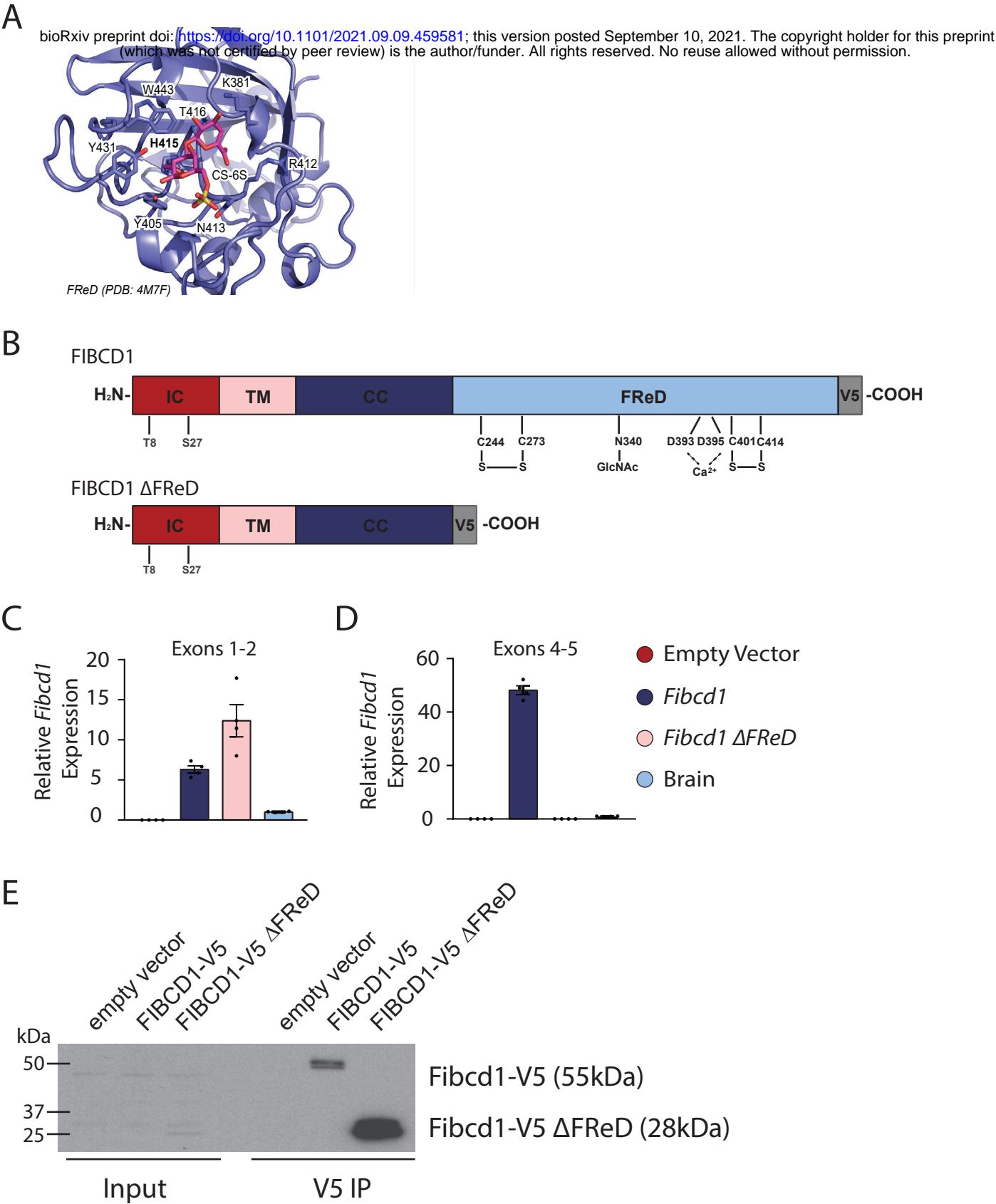
1032

1033

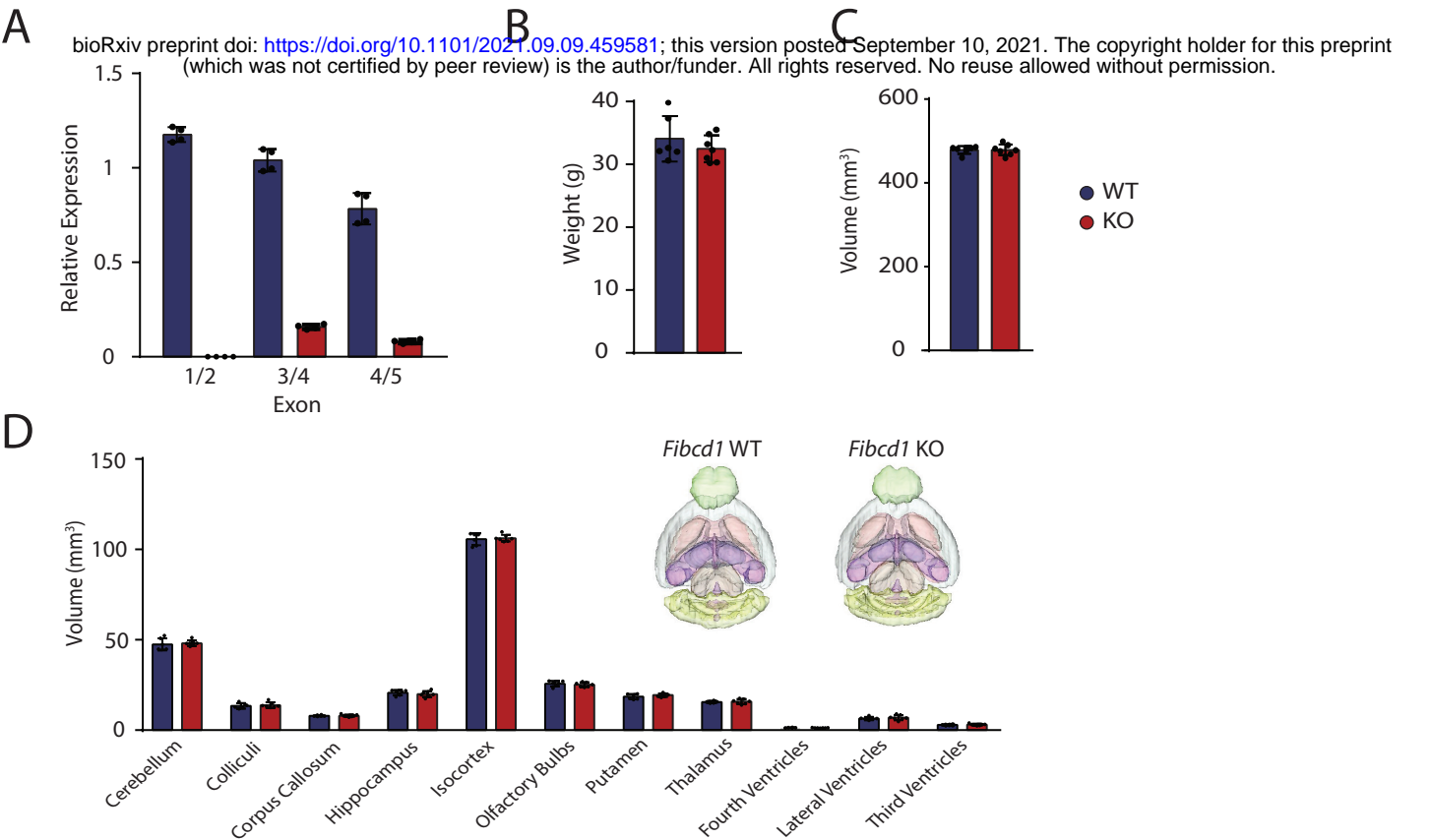
Supplemental Figure 1



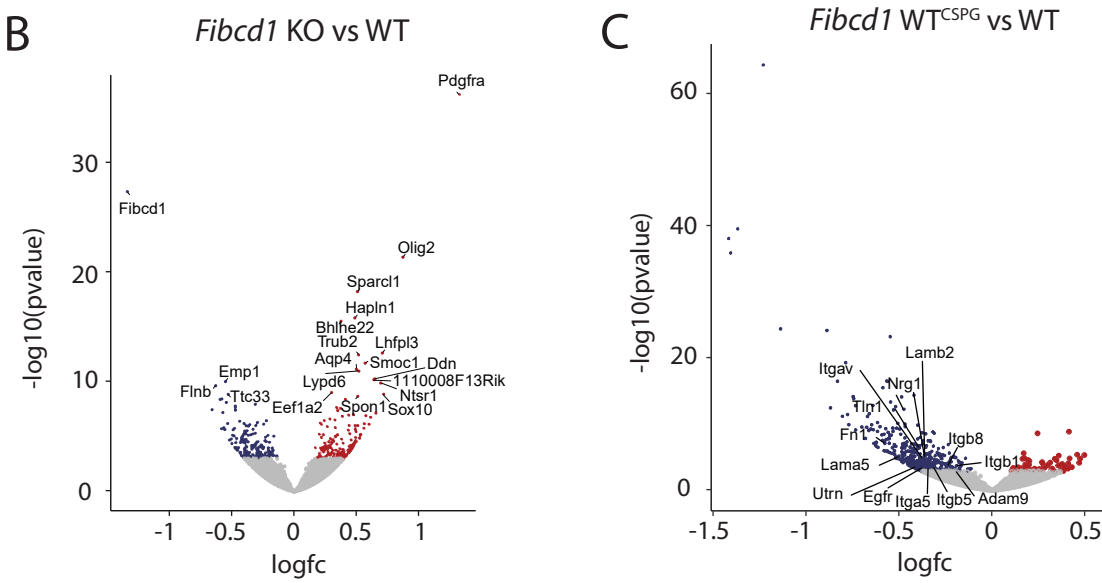
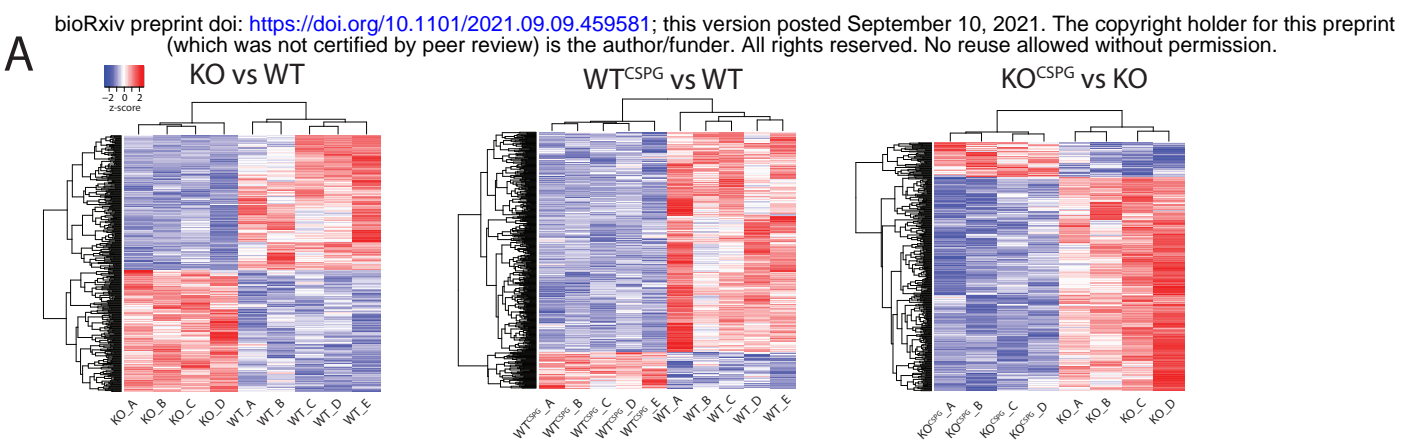
Supplemental Figure 2



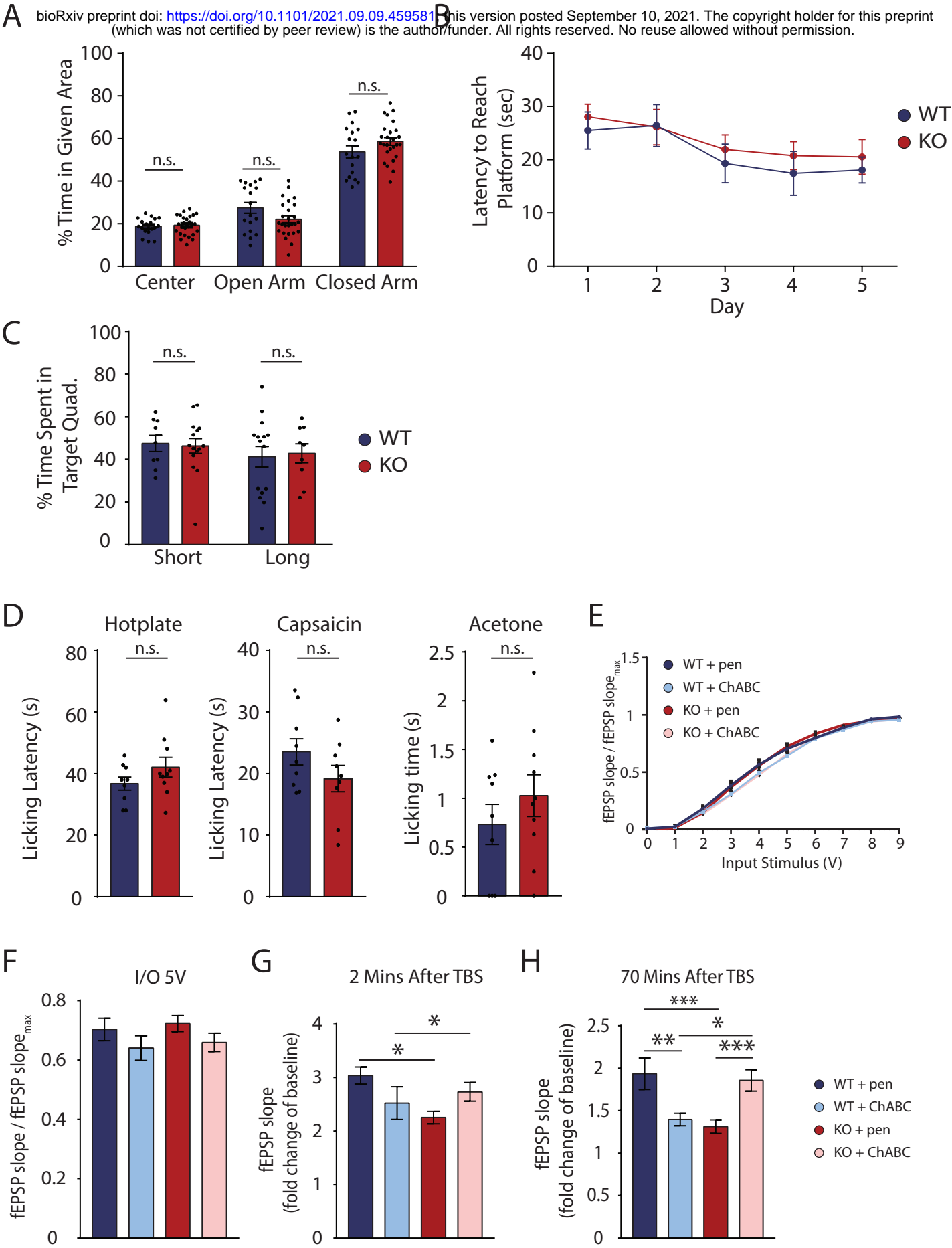
Supplemental Figure 3



Supplemental Figure 4



Supplemental Figure 5



Supplemental Figure 6

A bioRxiv preprint doi: <https://doi.org/10.1101/2021.09.09.459581>; this version posted September 10, 2021. The copyright holder for this preprint (which was not certified by peer review) is the author/funder. All rights reserved. No reuse allowed without permission.

CLUSTAL O(1.2.4) multiple sequence alignment

```
FRd_DROME  TATRQLPSSCSYSFLS----NHGILKVQLTPESFVYVSCD-----EDWTVLSRTSDDVNI 52
FRd_HUMAN  CATGSRPRDCLDVLVLSGQQDDGVYSVFPFTHYPAGFQVYCDHRTDGGGTVFQRRDGSVIN 60
FRd_MOUSE  CANGSRPRDCLDVLVLSGQQDDGVYSIFPTHYPAGFQVYCDHRTDGGGTVFQRRDGSVIN 60
          * . * . * : * : * : * : * : * : * : * : * : * : * : * : * : * : * : * :
          * : * : * : * : * : * : * : * : * : * : * : * : * : * : * : * : * : * :

FRd_DROME  FERGLDYRDGFGNLAGDFFIGLNLHALTSALHELRIVMEDFSGHVAAGYSLFAI-- 110
FRd_HUMAN  FFRGWDAYRDGFGRLTGEHMLGLKRIHALTTQAAAYELHVDLEDFENGTAAYARYGSFGVGL 120
FRd_MOUSE  FFRGWEAYREGFGKLTGEHMLGLKRIHALTTQAAAYELHVDLEDFNGTAYAHYGSFGVGL 120
          * * * * * : * : * : * : * : * : * : * : * : * : * : * : * : * : * : * :
          * : * : * : * : * : * : * : * : * : * : * : * : * : * : * : * : * : * :

FRd_DROME  --GSEKELYPLVLLGKFQDNLTSPAGDSLHYHAGAKFSTVDQDNDNCLCNCALRHKGA 167
FRd_HUMAN  FSDPPEEDGYPLTVA-----DYSGTAGDSLKHSQHRTTCKDRSDH-SENNCAAFYRGA 174
FRd_MOUSE  FSDPPEEDGYPLTVA-----DYSGTAGDSLKHSQHRTTCKDRSDH-SENNCAAFYRGA 174
          . * : * * : . : : * * * * * * : * : * : * : * : * : * : * : * : * :
          . * : * * : . : : * * * * * * : * : * : * : * : * : * : * : * : * :

FRd_DROME  GWFNCAKSNLFGYEYTTQNP-GETGIWMDTFSGQ-NSLKRVRWIRPIS 215
FRd_HUMAN  WMYRNCHTSNLNGQYLRGAHASYADGVESSWTGWQYSLKFSEMKIRPVR 224
FRd_MOUSE  WMYRNCHTSNLNGQYLRGAHASYADGVESSWTGWQYSLKFSEMKIRPVR 224
          * : * * * * * * : * : * : * * * * * * * : * : * : * : * : * : * :
          * : * * * * * * : * : * : * * * * * * * : * : * : * : * : * : * :
```

	DROME	HUMAN	MOUSE
DROME	100	41.63	40.19
HUMAN	41.63	100	96.88
MOUSE	40.19	96.88	100

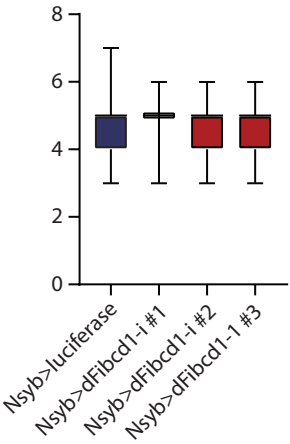
B

RNAi Line	Tub>Gal4 (Fullbody KD)	Nsyb>Gal4 (Neuronal KD)
UAS>CG10359 VDRC ¹⁰²⁶⁷⁰ (Line #1)	Viable	Viable*
UAS>CG10359 VDRC ⁴¹²⁸ (Line #2)	Semi-lethal	Viable*
UAS>CG10359 IR ^{BL63703} (Line #3)	Lethal	Viable*

* results in smaller larvae and skewed mendelian ratio

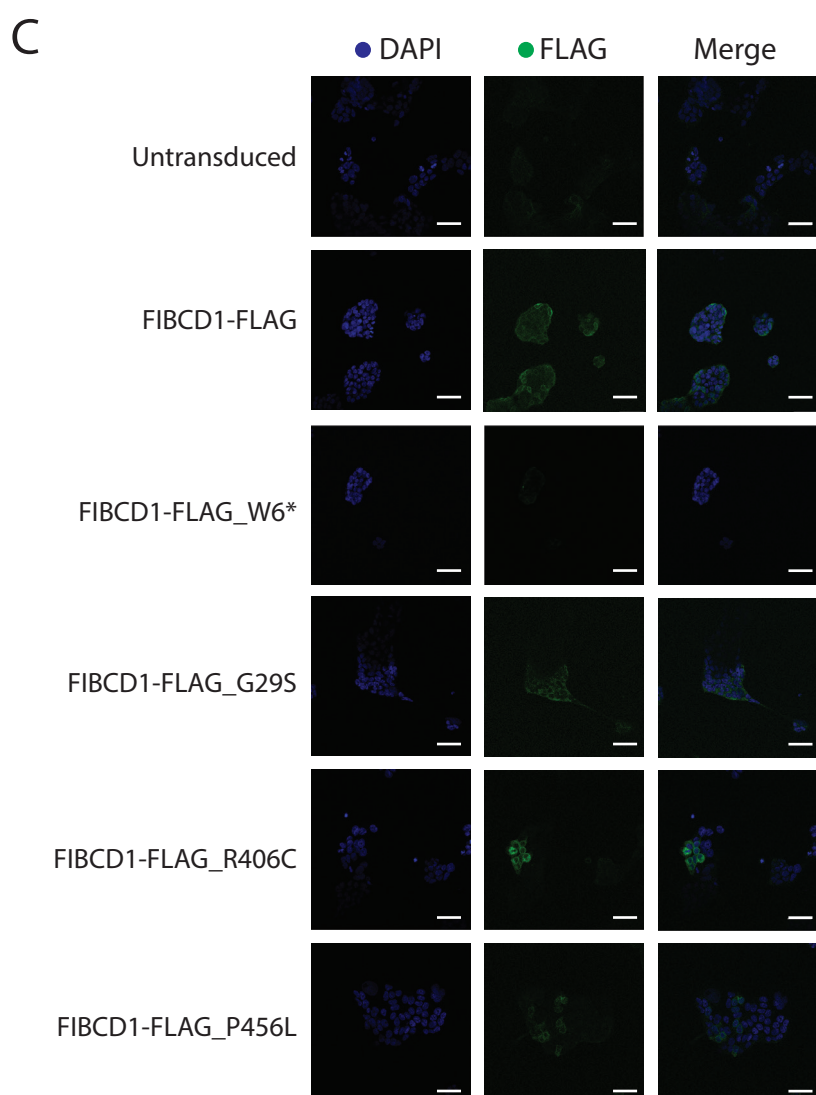
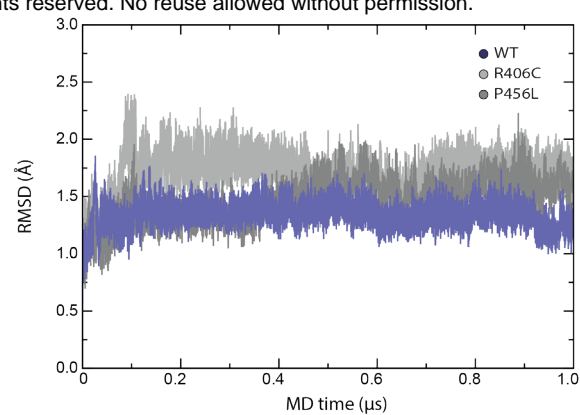
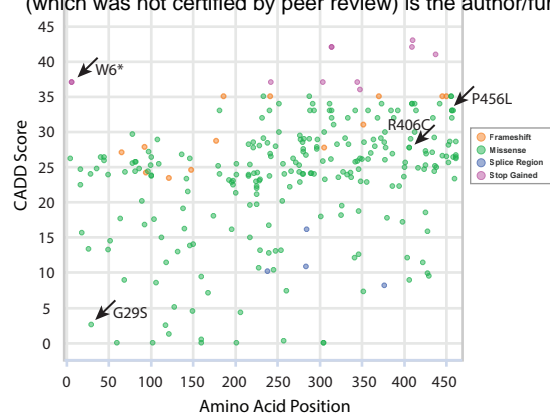
C

Climbing Assay - Sample Size per N



Supplemental Figure 7

A bioRxiv preprint doi: <https://doi.org/10.1101/2021.09.09.459581>; this version posted September 10, 2021. The copyright holder for this preprint (which was not certified by peer review) is the author/funder. All rights reserved. No reuse allowed without permission.



SUPPLEMENTARY FIGURE TITLES AND LEGENDS

Figure S1: *Fibcd1* expression in the adult and developing mouse brain.

(A) *Fibcd1* expression in bulk populations of sorted mouse brain cell population, from *brainrnaseq.org*. OPC = oligodendrocyte precursor cell. (B) Schematic of *Fibcd1* exons (grey rectangles) and introns (grey lines), and location of primer pair binding ('exons 1/2, 3/4 and 4/5') used for RT-qPCR. Exon sizes are to scale; introns and primer lengths are not. The exons coding for FIBCD1 FReD is indicated by a red dashed line. (C) Relative mRNA expression levels of *Fibcd1* (primers binding to exon 1 and 2) normalised to *Gapdh* in the indicated brain regions, analysed by RT-qPCR (N = 3). (D) Relative mRNA expression levels of *Fibcd1* (primers binding to exon 1 and 2 and exons 3 and 4) normalised to *Gapdh* in the hippocampus of the indicated time points, analysed by RT-qPCR (N = 3). Error bars represent SD.

Figure S2: Docking site of CS-6S in FIBCD1 FReD and validation of mFIBCD1 overexpressing N2a cell lines.

(A) Top binding pose for *in silico* docking of CS-6S to FIBCD1 FReD (PDB 4M7F). (B) Schematic representation of FIBCD1 domains, IC-intracellular domain (red), TM-transmembrane domain (pink), CC-coiled coil domain (dark blue), FReD (light blue), and location of V5-tag (grey) in full-length mFIBCD1 cDNA and truncated mFIBCD1 lacking the FReD domain (FIBCD1 Δ FReD). (C) Relative mRNA expression levels of *Fibcd1* in the N2a cells overexpressing full-length (*Fibcd1*) or truncated *FIBCD1* (*Fibcd1* Δ FReD) and adult mouse WT brain for comparison, analysed by RT-qPCR (n = 2). Primers binding to exon 1 and 2 before the FReD domain (B) or to exon 4 and 5 spanning the sequence encoding part of the FReD. Note the complete absence of endogenous *Fibcd1* expression in the 'empty vector' (red bar) control and the complete absence of expression when using primers against exon 4/5 (D), which span the FReD (see Figure S1B) in the *Fibcd1* Δ FReD construct (C, pink bar), validating

the generated cell lines. *Gapdh* was used as housekeeping control and values obtained from a control brain sample were set to 1. (E) Validation of transgenic N2a cell line at the protein level by immunoprecipitation with anti-V5 antibody as bait. Input (left) and V5-immunoprecipitated (right) lysates from N2a cells expressing V5-tagged full-length mFIBCD1 (mFIBCD1-V5, predicted size of 55kDa), V5-tagged mFIBCD1 lacking the FReD (V5-FIBCD1 Δ FReD, predicted size of 28kDa) or the empty vector as negative control. Protein marker sizes are indicated.

Figure S3: *Fibcd1* expression, weight and brain tissue volumes in *Fibcd1* WT and KO mice.

(A) RT-qPCR of *Fibcd1* WT and KO adult mouse hippocampi using primer pairs binding to indicated exons (see Fig. S1B). N = 4. (B-D) Body weight (B), total brain volume (C) and brain volumes of denoted brain regions (D) of the indicated genotypes as assessed by MRI volumetric analysis (N > 5). Inset are 3D representative MRI renditions of control (left) and *Fibcd1* KO (right) adult brains with analysed brain regions pseudo-coloured. Error bars represent SD.

Figure S4: Additional RNA-seq analysis

(A) z-score hierarchical clustering for each sample in *Fibcd1* KO vs WT, WT^{CSPG} vs WT and KO^{CSPG} vs KO. Colours represent scaled expression values, with blue for low and red for high expression levels. Legend is indicated. (B) Volcano plot depicting differential gene expression at DIV2 hippocampal cultures, comparing *Fibcd1* KO vs WT, showing significantly upregulated (red) and downregulated (blue) genes. Top 20 differentially expressed genes are labelled. (C) Volcano plot depicting differential gene expression at DIV2 hippocampal cultures comparing WT^{CSPG} vs WT, all genes that fall into “integrin binding” GO term category are labelled.

Figure S5: Analysis of *Fibcd1* KO mouse neurological phenotype.

(A) Percentage of time mice spent in the centre, open and closed arms of the Elevated Plus Maze (EPM) are shown for *Fibcd1* WT (blue) and KO (red). N = 18 WT; 27 KO. (B-C) Mouse performance quantified by time to reach the target platform (B) and time spent in the target quadrant (C), in Morris Water Maze (MWM) hippocampal-dependent spatial learning task over 5 days. N = 5 WT; 9 KO. (D) Acute pain responses to hotplate, acetone drop, or intraplantar capsaicin injections, quantified as time to first response or time spent licking or biting the injected paw, respectively. N = 9 WT; N = 10 KO. (E-F) Input/output assessment of synaptic transmission in CA3-CA1 Schaffer collateral pathway of adult mouse hippocampal slices. *Fibcd1* WT (blue) and KO (red) hippocampal slices, pre-treated with penicillinase (pen) or Chondroitinase ABC (ChABC). N (WT+pen) = 22; N (KO+pen) = 27; N (WT+ChABC) = 21; N (KO+ChABC) = 30. (G-H) LTP fold change of baseline at 2 (G) and 70 (H) minutes post theta-burst stimulation (TBS) in adult mouse hippocampal slices. N (WT+pen) = 9; N (KO+pen) = 15; N (WT+ChABC) = 6; N (KO+ChABC) = 12. Not significant, n.s., * = $p \leq 0.05$; ** = $p \leq 0.01$; *** = $p \leq 0.001$. Error bars represent SEM.

Figure S6: Description of *dFibcd1*.

(A) Alignment of human, mouse and fly (DROME) FReD protein sequence. Inset, percent identity matrix (% homology) between Drosophila, human and mouse FReD protein sequences. (B) Summary of 3 RNAi lines crossed to full body GAL4 driver (tubulin) or neuron-specific (Nsyb) and the effects on viability. (C) Number of flies analysed for the climbing assay in Fig 4I.

Figure S7: Additional human *Fibcd1* data.

(A) Missense, frameshift, splice region and stop gain variants present in the population. Each dot represents one distinct variants, amino acid position and CADD score indicated on x and y axis. Indicated with arrows are the variants discussed in the present study. Data originally from gnomAD. (B) Time course of the backbone RMSD from the starting configuration for WT (blue), R406C (pink) and P456L (red) MD simulations. (C) Validation of FIBCD1 expression in stably expressing HEK293t cells by immunofluorescence. Shown is DAPI (blue), anti-FLAG (green) and merge. Scale bar = 50um.

REFERENCES

- 1 Dityatev, A., Schachner, M. & Sonderegger, P. The dual role of the extracellular matrix in synaptic plasticity and homeostasis. *Nat Rev Neurosci* **11**, 735-746, doi:10.1038/nrn2898 (2010).
- 2 Smith, P. D., Coulson-Thomas, V. J., Foscarin, S., Kwok, J. C. & Fawcett, J. W. "GAG-ing with the neuron": The role of glycosaminoglycan patterning in the central nervous system. *Exp Neurol* **274**, 100-114, doi:10.1016/j.expneurol.2015.08.004 (2015).
- 3 Carulli, D., Laabs, T., Geller, H. M. & Fawcett, J. W. Chondroitin sulfate proteoglycans in neural development and regeneration. *Curr Opin Neurobiol* **15**, 116-120, doi:10.1016/j.conb.2005.01.014 (2005).
- 4 Dityatev, A. & Schachner, M. Extracellular matrix molecules and synaptic plasticity. *Nat Rev Neurosci* **4**, 456-468, doi:10.1038/nrn1115 (2003).
- 5 Freeze, H. H., Eklund, E. A., Ng, B. G. & Patterson, M. C. Neurology of inherited glycosylation disorders. *Lancet Neurol* **11**, 453-466, doi:10.1016/S1474-4422(12)70040-6 (2012).
- 6 Freeze, H. H., Eklund, E. A., Ng, B. G. & Patterson, M. C. Neurological aspects of human glycosylation disorders. *Annu Rev Neurosci* **38**, 105-125, doi:10.1146/annurev-neuro-071714-034019 (2015).
- 7 Dwyer, C. A. & Esko, J. D. Glycan susceptibility factors in autism spectrum disorders. *Mol Aspects Med* **51**, 104-114, doi:10.1016/j.mam.2016.07.001 (2016).
- 8 Kitagawa, H., Tsutsumi, K., Tone, Y. & Sugahara, K. Developmental regulation of the sulfation profile of chondroitin sulfate chains in the chicken embryo brain. *J Biol Chem* **272**, 31377-31381, doi:10.1074/jbc.272.50.31377 (1997).
- 9 Miller, G. M. & Hsieh-Wilson, L. C. Sugar-dependent modulation of neuronal development, regeneration, and plasticity by chondroitin sulfate proteoglycans. *Exp Neurol* **274**, 115-125, doi:10.1016/j.expneurol.2015.08.015 (2015).
- 10 Sorg, B. A. *et al.* Casting a Wide Net: Role of Perineuronal Nets in Neural Plasticity. *J Neurosci* **36**, 11459-11468, doi:10.1523/JNEUROSCI.2351-16.2016 (2016).
- 11 Gogolla, N., Caroni, P., Luthi, A. & Herry, C. Perineuronal nets protect fear memories from erasure. *Science* **325**, 1258-1261, doi:10.1126/science.1174146 (2009).
- 12 Dickendesher, T. L. *et al.* NgR1 and NgR3 are receptors for chondroitin sulfate proteoglycans. *Nat Neurosci* **15**, 703-712, doi:10.1038/nn.3070 (2012).
- 13 Shen, Y. *et al.* PTPsigma is a receptor for chondroitin sulfate proteoglycan, an inhibitor of neural regeneration. *Science* **326**, 592-596, doi:10.1126/science.1178310 (2009).
- 14 Xu, B. *et al.* Role of CSPG receptor LAR phosphatase in restricting axon regeneration after CNS injury. *Neurobiol Dis* **73**, 36-48, doi:10.1016/j.nbd.2014.08.030 (2015).
- 15 Mikami, T., Yasunaga, D. & Kitagawa, H. Contactin-1 is a functional receptor for neuroregulatory chondroitin sulfate-E. *J Biol Chem* **284**, 4494-4499, doi:10.1074/jbc.M809227200 (2009).
- 16 Mizumoto, S., Takahashi, J. & Sugahara, K. Receptor for advanced glycation end products (RAGE) functions as receptor for specific sulfated glycosaminoglycans, and anti-RAGE antibody or sulfated glycosaminoglycans delivered in vivo inhibit pulmonary metastasis of tumor cells. *J Biol Chem* **287**, 18985-18994, doi:10.1074/jbc.M111.313437 (2012).
- 17 Donahue, J. E. *et al.* RAGE, LRP-1, and amyloid-beta protein in Alzheimer's disease. *Acta Neuropathol* **112**, 405-415, doi:10.1007/s00401-006-0115-3 (2006).
- 18 Schlosser, A. *et al.* Characterization of FIBCD1 as an acetyl group-binding receptor that binds chitin. *J Immunol* **183**, 3800-3809, doi:10.4049/jimmunol.0901526 (2009).

- 1169 19 Moeller, J. B. *et al.* Modulation of the fungal mycobiome is regulated by the chitin-binding receptor FIBCD1. *J Exp Med* **216**, 2689-2700, doi:10.1084/jem.20182244 (2019).
- 1170
- 1171
- 1172 20 Thomsen, T. *et al.* The recognition unit of FIBCD1 organizes into a noncovalently linked tetrameric structure and uses a hydrophobic funnel (S1) for acetyl group recognition. *J Biol Chem* **285**, 1229-1238, doi:10.1074/jbc.M109.061523 (2010).
- 1173
- 1174
- 1175 21 Shrive, A. K. *et al.* Crystal structure of the tetrameric fibrinogen-like recognition domain of fibrinogen C domain containing 1 (FIBCD1) protein. *J Biol Chem* **289**, 2880-2887, doi:10.1074/jbc.M113.520577 (2014).
- 1176
- 1177
- 1178 22 Zhang, Y. *et al.* Purification and Characterization of Progenitor and Mature Human Astrocytes Reveals Transcriptional and Functional Differences with Mouse. *Neuron* **89**, 37-53, doi:10.1016/j.neuron.2015.11.013 (2016).
- 1179
- 1180
- 1181 23 Soares da Costa, D., Reis, R. L. & Pashkuleva, I. Sulfation of Glycosaminoglycans and Its Implications in Human Health and Disorders. *Annu Rev Biomed Eng* **19**, 1-26, doi:10.1146/annurev-bioeng-071516-044610 (2017).
- 1182
- 1183
- 1184 24 Miyata, S. & Kitagawa, H. Chondroitin 6-Sulfation Regulates Perineuronal Net Formation by Controlling the Stability of Aggrecan. *Neural Plast* **2016**, 1305801, doi:10.1155/2016/1305801 (2016).
- 1185
- 1186
- 1187 25 Miyata, S., Komatsu, Y., Yoshimura, Y., Taya, C. & Kitagawa, H. Persistent cortical plasticity by upregulation of chondroitin 6-sulfation. *Nat Neurosci* **15**, 414-422, S411-412, doi:10.1038/nn.3023 (2012).
- 1188
- 1189
- 1190 26 Ribeiro Ede, A., Jr. *et al.* The structure and regulation of human muscle alpha-actinin. *Cell* **159**, 1447-1460, doi:10.1016/j.cell.2014.10.056 (2014).
- 1191
- 1192 27 Kurkcuoglu, Z. *et al.* Performance of HADDOCK and a simple contact-based protein-ligand binding affinity predictor in the D3R Grand Challenge 2. *J Comput Aided Mol Des* **32**, 175-185, doi:10.1007/s10822-017-0049-y (2018).
- 1193
- 1194
- 1195 28 Jin, J. *et al.* Effect of chondroitin sulfate proteoglycans on neuronal cell adhesion, spreading and neurite growth in culture. *Neural Regen Res* **13**, 289-297, doi:10.4103/1673-5374.226398 (2018).
- 1196
- 1197
- 1198 29 Tang, T. *et al.* A mouse knockout library for secreted and transmembrane proteins. *Nat Biotechnol* **28**, 749-755, doi:10.1038/nbt.1644 (2010).
- 1199
- 1200 30 Zhao, R. R. & Fawcett, J. W. Combination treatment with chondroitinase ABC in spinal cord injury--breaking the barrier. *Neurosci Bull* **29**, 477-483, doi:10.1007/s12264-013-1359-2 (2013).
- 1201
- 1202
- 1203 31 Bray, E. R. *et al.* Thrombospondin-1 Mediates Axon Regeneration in Retinal Ganglion Cells. *Neuron* **103**, 642-657 e647, doi:10.1016/j.neuron.2019.05.044 (2019).
- 1204
- 1205 32 Collins-Racie, L. A. *et al.* ADAMTS-8 exhibits aggrecanase activity and is expressed in human articular cartilage. *Matrix Biol* **23**, 219-230, doi:10.1016/j.matbio.2004.05.004 (2004).
- 1206
- 1207
- 1208 33 Nieswandt, B. *et al.* Loss of talin1 in platelets abrogates integrin activation, platelet aggregation, and thrombus formation in vitro and in vivo. *J Exp Med* **204**, 3113-3118, doi:10.1084/jem.20071827 (2007).
- 1209
- 1210
- 1211 34 Yoshino, Y. *et al.* Targeted deletion of HYBID (hyaluronan binding protein involved in hyaluronan depolymerization/ KIAA1199/CEMIP) decreases dendritic spine density in the dentate gyrus through hyaluronan accumulation. *Biochem Biophys Res Commun* **503**, 1934-1940, doi:10.1016/j.bbrc.2018.07.138 (2018).
- 1212
- 1213
- 1214
- 1215 35 Begay, R. L. *et al.* Filamin C Truncation Mutations Are Associated With Arrhythmogenic Dilated Cardiomyopathy and Changes in the Cell-Cell Adhesion Structures. *JACC Clin Electrophysiol* **4**, 504-514, doi:10.1016/j.jacep.2017.12.003 (2018).
- 1216
- 1217
- 1218

- 1219 36 Desnoyers, L., Arnott, D. & Pennica, D. WISP-1 binds to decorin and biglycan. *J Biol*
1220 *Chem* **276**, 47599-47607, doi:10.1074/jbc.M108339200 (2001).
- 1221 37 Manso, A. M. *et al.* Loss of mouse cardiomyocyte talin-1 and talin-2 leads to beta-1
1222 integrin reduction, costameric instability, and dilated cardiomyopathy. *Proc Natl Acad*
1223 *Sci U S A* **114**, E6250-E6259, doi:10.1073/pnas.1701416114 (2017).
- 1224 38 Haage, A. *et al.* Talin Autoinhibition Regulates Cell-ECM Adhesion Dynamics and
1225 Wound Healing In Vivo. *Cell Rep* **25**, 2401-2416 e2405,
1226 doi:10.1016/j.celrep.2018.10.098 (2018).
- 1227 39 Slaker, M. *et al.* Removal of perineuronal nets in the medial prefrontal cortex impairs
1228 the acquisition and reconsolidation of a cocaine-induced conditioned place preference
1229 memory. *J Neurosci* **35**, 4190-4202, doi:10.1523/JNEUROSCI.3592-14.2015 (2015).
- 1230 40 Bruckner, G. *et al.* Acute and long-lasting changes in extracellular-matrix chondroitin-
1231 sulphate proteoglycans induced by injection of chondroitinase ABC in the adult rat
1232 brain. *Exp Brain Res* **121**, 300-310, doi:10.1007/s002210050463 (1998).
- 1233 41 Vegh, M. J. *et al.* Hippocampal extracellular matrix levels and stochasticity in
1234 synaptic protein expression increase with age and are associated with age-dependent
1235 cognitive decline. *Mol Cell Proteomics* **13**, 2975-2985,
1236 doi:10.1074/mcp.M113.032086 (2014).
- 1237 42 Yang, S. *et al.* Perineuronal net digestion with chondroitinase restores memory in
1238 mice with tau pathology. *Exp Neurol* **265**, 48-58, doi:10.1016/j.expneurol.2014.11.013
1239 (2015).
- 1240 43 Wilson, M. A. & Tonegawa, S. Synaptic plasticity, place cells and spatial memory:
1241 study with second generation knockouts. *Trends Neurosci* **20**, 102-106,
1242 doi:10.1016/s0166-2236(96)01023-5 (1997).
- 1243 44 Bukalo, O., Schachner, M. & Dityatev, A. Modification of extracellular matrix by
1244 enzymatic removal of chondroitin sulfate and by lack of tenascin-R differentially
1245 affects several forms of synaptic plasticity in the hippocampus. *Neuroscience* **104**,
1246 359-369, doi:10.1016/s0306-4522(01)00082-3 (2001).
- 1247 45 Nicoll, R. A. & Malenka, R. C. Expression mechanisms underlying NMDA receptor-
1248 dependent long-term potentiation. *Ann N Y Acad Sci* **868**, 515-525,
1249 doi:10.1111/j.1749-6632.1999.tb11320.x (1999).
- 1250 46 Kochlamazashvili, G. *et al.* The extracellular matrix molecule hyaluronic acid
1251 regulates hippocampal synaptic plasticity by modulating postsynaptic L-type Ca(2+)
1252 channels. *Neuron* **67**, 116-128, doi:10.1016/j.neuron.2010.05.030 (2010).
- 1253 47 Karczewski, K. J. *et al.* The mutational constraint spectrum quantified from variation
1254 in 141,456 humans. *Nature* **581**, 434-443, doi:10.1038/s41586-020-2308-7 (2020).
- 1255 48 Sobreira, N., Schiettecatte, F., Valle, D. & Hamosh, A. GeneMatcher: a matching tool
1256 for connecting investigators with an interest in the same gene. *Hum Mutat* **36**, 928-
1257 930, doi:10.1002/humu.22844 (2015).
- 1258 49 Wu, J. *et al.* Genomic landscapes of Chinese sporadic autism spectrum disorders
1259 revealed by whole-genome sequencing. *J Genet Genomics* **45**, 527-538,
1260 doi:10.1016/j.jgg.2018.09.002 (2018).
- 1261 50 Unlu, G. *et al.* Phenome-based approach identifies RIC1-linked Mendelian syndrome
1262 through zebrafish models, biobank associations and clinical studies. *Nat Med* **26**, 98-
1263 109, doi:10.1038/s41591-019-0705-y (2020).
- 1264 51 Patel, N. *et al.* Novel phenotypes and loci identified through clinical genomics
1265 approaches to pediatric cataract. *Hum Genet* **136**, 205-225, doi:10.1007/s00439-016-
1266 1747-6 (2017).
- 1267 52 Wang, J. *et al.* UNC13B variants associated with partial epilepsy with favourable
1268 outcome. *Brain*, doi:10.1093/brain/awab164 (2021).

- 1269 53 Thomsen, T., Schlosser, A., Holmskov, U. & Sorensen, G. L. Ficolins and FIBCD1:
1270 soluble and membrane bound pattern recognition molecules with acetyl group
1271 selectivity. *Mol Immunol* **48**, 369-381, doi:10.1016/j.molimm.2010.09.019 (2011).
- 1272 54 Jepsen, C. S. *et al.* FIBCD1 Binds Aspergillus fumigatus and Regulates Lung
1273 Epithelial Response to Cell Wall Components. *Front Immunol* **9**, 1967,
1274 doi:10.3389/fimmu.2018.01967 (2018).
- 1275 55 Retterer, K. *et al.* Clinical application of whole-exome sequencing across clinical
1276 indications. *Genet Med* **18**, 696-704, doi:10.1038/gim.2015.148 (2016).
- 1277 56 Yan, H. *et al.* Genetic analysis of 20 patients with hypomyelinating leukodystrophy by
1278 trio-based whole-exome sequencing. *J Hum Genet* **66**, 761-768, doi:10.1038/s10038-
1279 020-00896-5 (2021).
- 1280 57 Zhang, P. *et al.* PopViz: a webserver for visualizing minor allele frequencies and
1281 damage prediction scores of human genetic variations. *Bioinformatics* **34**, 4307-4309,
1282 doi:10.1093/bioinformatics/bty536 (2018).
- 1283 58 Lassen, N. E. *et al.* Coupling of Bone Resorption and Formation in Real Time: New
1284 Knowledge Gained From Human Haversian BMUs. *J Bone Miner Res* **32**, 1395-1405,
1285 doi:10.1002/jbmr.3091 (2017).
- 1286 59 Love, M. I., Huber, W. & Anders, S. Moderated estimation of fold change and
1287 dispersion for RNA-seq data with DESeq2. *Genome Biol* **15**, 550,
1288 doi:10.1186/s13059-014-0550-8 (2014).
- 1289 60 Jalili, V. *et al.* The Galaxy platform for accessible, reproducible and collaborative
1290 biomedical analyses: 2020 update. *Nucleic Acids Res* **48**, W395-W402,
1291 doi:10.1093/nar/gkaa434 (2020).
- 1292 61 Liao, Y., Wang, J., Jaehnig, E. J., Shi, Z. & Zhang, B. WebGestalt 2019: gene set
1293 analysis toolkit with revamped UIs and APIs. *Nucleic Acids Res* **47**, W199-W205,
1294 doi:10.1093/nar/gkz401 (2019).
- 1295 62 Jones, G., Willett, P., Glen, R. C., Leach, A. R. & Taylor, R. Development and
1296 validation of a genetic algorithm for flexible docking. *J Mol Biol* **267**, 727-748,
1297 doi:10.1006/jmbi.1996.0897 (1997).
- 1298 63 van Zundert, G. C. P. *et al.* The HADDOCK2.2 Web Server: User-Friendly
1299 Integrative Modeling of Biomolecular Complexes. *J Mol Biol* **428**, 720-725,
1300 doi:10.1016/j.jmb.2015.09.014 (2016).
- 1301 64 Schrodinger, LLC. *The PyMOL Molecular Graphics System, Version 1.8* (2015).
- 1302 65 Abraham, M. J. *et al.* GROMACS: High performance molecular simulations through
1303 multi-level parallelism from laptops to supercomputers. *SoftwareX* **1-2**, 19-25,
1304 doi:<https://doi.org/10.1016/j.softx.2015.06.001> (2015).
- 1305 66 Lindorff-Larsen, K. *et al.* Improved side-chain torsion potentials for the Amber
1306 ff99SB protein force field. *Proteins* **78**, 1950-1958, doi:10.1002/prot.22711 (2010).
- 1307 67 Jorgensen, W. L. Quantum and statistical mechanical studies of liquids. 10.
1308 Transferable intermolecular potential functions for water, alcohols, and ethers.
1309 Application to liquid water. *Journal of the American Chemical Society* **103**, 335-340,
1310 doi:10.1021/ja00392a016 (1981).
- 1311 68 Hoover, W. G. Canonical dynamics: Equilibrium phase-space distributions. *Phys Rev*
1312 *A Gen Phys* **31**, 1695-1697, doi:10.1103/physreva.31.1695 (1985).
- 1313 69 Parrinello, M. & Rahman, A. Polymorphic transitions in single crystals: A new
1314 molecular dynamics method. *Journal of Applied Physics* **52**, 7182-7190,
1315 doi:10.1063/1.328693 (1981).
- 1316 70 Hess, B., Bekker, H., Berendsen, H. J. C. & Fraaije, J. G. E. M. LINCS: A linear
1317 constraint solver for molecular simulations. *Journal of Computational Chemistry* **18**,
1318 1463-1472, doi:[https://doi.org/10.1002/\(SICI\)1096-987X\(199709\)18:12<1463::AID-](https://doi.org/10.1002/(SICI)1096-987X(199709)18:12<1463::AID-JCC4>3.0.CO;2-H)
1319 [JCC4>3.0.CO;2-H](https://doi.org/10.1002/(SICI)1096-987X(199709)18:12<1463::AID-JCC4>3.0.CO;2-H) (1997).

- 1320 71 Jurrus, E. *et al.* Improvements to the APBS biomolecular solvation software suite.
1321 *Protein Sci* **27**, 112-128, doi:10.1002/pro.3280 (2018).
- 1322 72 Nagy, V. *et al.* HACE1 deficiency leads to structural and functional
1323 neurodevelopmental defects. *Neurol Genet* **5**, e330,
1324 doi:10.1212/NXG.0000000000000330
1325 NG2018008979 [pii] (2019).
- 1326 73 Paxinos, G. & Watson, C. *The rat brain in stereotaxic coordinates: hard cover*
1327 *edition*. (Elsevier, 2006).
- 1328 74 Takegawa, Y. *et al.* Simultaneous analysis of heparan sulfate, chondroitin/dermatan
1329 sulfates, and hyaluronan disaccharides by glycoblotting-assisted sample preparation
1330 followed by single-step zwitter-ionic-hydrophilic interaction chromatography. *Anal*
1331 *Chem* **83**, 9443-9449, doi:10.1021/ac2021079 (2011).
- 1332 75 Cicvaric, A. *et al.* Enhanced synaptic plasticity and spatial memory in female but not
1333 male FLRT2-haplodeficient mice. *Sci Rep* **8**, 3703, doi:10.1038/s41598-018-22030-4
1334 (2018).
- 1335 76 Cicvaric, A. *et al.* The brain-tumor related protein podoplanin regulates synaptic
1336 plasticity and hippocampus-dependent learning and memory. *Ann Med* **48**, 652-668,
1337 doi:10.1080/07853890.2016.1219455 (2016).
- 1338 77 Rammes, G. *et al.* Isoflurane anaesthesia reversibly improves cognitive function and
1339 long-term potentiation (LTP) via an up-regulation in NMDA receptor 2B subunit
1340 expression. *Neuropharmacology* **56**, 626-636 (2009).
- 1341 78 Simon, W., Hapfelmeier, G., Kochs, E., Zieglgansberger, W. & Rammes, G.
1342 Isoflurane blocks synaptic plasticity in the mouse hippocampus. *Anesthesiology* **94**,
1343 1058-1065 (2001).
- 1344 79 Monje, F. J. *et al.* Focal adhesion kinase regulates neuronal growth, synaptic plasticity
1345 and hippocampus-dependent spatial learning and memory. *Neuro-Signals* **20**, 1-14
1346 (2012).
- 1347 80 Kim, E. J. *et al.* Alzheimer's disease risk factor lymphocyte-specific protein tyrosine
1348 kinase regulates long-term synaptic strengthening, spatial learning and memory. *Cell*
1349 *Mol Life Sci* (2012).
- 1350 81 Sievers, F. *et al.* Fast, scalable generation of high-quality protein multiple sequence
1351 alignments using Clustal Omega. *Mol Syst Biol* **7**, 539, doi:10.1038/msb.2011.75
1352 (2011).
- 1353